JGR Solid Earth

RESEARCH ARTICLE
10.1029/2023JB026415

Improved Characterization of Ultralow-Velocity Zones Through Advances in Bayesian Inversion of ScP Waveforms

Surya Pachhai[1], **Michael S. Thorne**[1], **and Sebastian Rost**[2]

[1]Department of Geology and Geophysics, University of Utah, Salt Lake City, UT, USA, [2]School of Earth and Environment, Institute of Geophysics and Tectonics, University of Leeds, Leeds, UK

Key Points:

- We developed a Bayesian waveform inversion approach that combines ScP arrivals from multiple events and incorporates path attenuation
- Failure to include attenuation in the inversion can yield incorrect ultralow-velocity zone (ULVZ) elastic parameters
- Lateral variation of ULVZ parameters beneath the Coral Sea may be affected by 2-/3-D ULVZ shape

Supporting Information:

Supporting Information may be found in the online version of this article.

Correspondence to:

S. Pachhai,
surya.pachhai@utah.edu

Citation:

Pachhai, S., Thorne, M. S., & Rost, S. (2023). Improved characterization of ultralow-velocity zones through advances in Bayesian inversion of ScP waveforms. *Journal of Geophysical Research: Solid Earth*, *128*, e2023JB026415. https://doi.org/10.1029/2023JB026415

Received 13 JAN 2023
Accepted 12 JUN 2023

Author Contributions:

Conceptualization: Surya Pachhai, Michael S. Thorne, Sebastian Rost
Data curation: Surya Pachhai
Formal analysis: Surya Pachhai, Michael S. Thorne, Sebastian Rost
Funding acquisition: Michael S. Thorne, Sebastian Rost
Methodology: Surya Pachhai
Software: Surya Pachhai, Michael S. Thorne
Validation: Surya Pachhai, Michael S. Thorne, Sebastian Rost
Visualization: Surya Pachhai, Michael S. Thorne

Abstract Ultralow-velocity zones (ULVZs) have been studied using a variety of seismic phases; however, their physical origin is still poorly understood. Short period ScP waveforms are extensively used to infer ULVZ properties because they may be sensitive to all ULVZ elastic moduli and thickness. However, ScP waveforms are additionally complicated by the effects of path attenuation, coherent noise, and source complexity. To address these complications, we developed a hierarchical Bayesian inversion method that allows us to invert ScP waveforms from multiple events simultaneously and accounts for path attenuation and correlated noise. The inversion method is tested with synthetic predictions which show that the inclusion of attenuation is imperative to recover ULVZ parameters accurately and that the ULVZ thickness and S-wave velocity decrease are most reliably recovered. Utilizing multiple events simultaneously reduces the effects of coherent noise and source time function complexity, which in turn allows for the inclusion of more data to be used in the analyses. We next applied the method to ScP data recorded in Australia for 291 events that sample the core-mantle boundary beneath the Coral Sea. Our results indicate, on average, ~12-km thick ULVZ with ~14% reduction in S-wave velocity across the region, but there is a greater variability in ULVZ properties in the south than that in the north of the sampled region. P-wave velocity reductions and density perturbations are mostly below 10%. These ScP data show more than one ScP post-cursor in some areas which may indicate complex 3-D ULVZ structures.

Plain Language Summary Studies of the Earth's deep interior using seismic energy generated by earthquakes show the presence of small-scale structures at the core-mantle boundary (CMB) known as ultralow-velocity zones (ULVZs). The seismic waves traveling through these features are inferred to be slowed down by as much as 50% with respect to normal mantle material. However, it is challenging to determine the physical composition of these ULVZs and how they are linked to other structures in the Earth's interior because we don't have precise knowledge on their physical properties. To understand their origins, we need to estimate their physical properties (i.e., velocity and density) as accurately as possible. This study focuses on the development and application of a probabilistic approach that can provide an unbiased estimate of seismic velocity and density. Our new approach can take data from multiple events simultaneously and incorporates data noise and possible absorption of seismic energy along the path. Application of this approach to real data that sample the CMB beneath the Coral Sea show a wide spread ULVZ with much less lateral variation in material parameters in comparison to solutions using single events. We also find observations that may be linked to 3-D ULVZ structure.

1. Introduction

Resolving the elastic properties of the deep Earth provides crucial information about material properties and ongoing dynamic processes in this inaccessible part of our planet. Seismic velocity and density have been extensively imaged using travel-times and/or waveform modeling of a wide variety of seismic phases and normal mode spectra, demonstrating that the lowermost mantle is one of the most complex regions in the Earth's interior (Garnero, 2000; Garnero et al., 2016; Lay & Garnero, 2011; McNamara, 2019). Over the last several decades increases in computational power have spurred the development of more sophisticated seismic analysis methods, which, combined with an ever-growing volume of high-quality seismic data, have revealed an array of complex structures in the lowermost mantle at several length scales. At the largest length-scale (>1,000 km) two nearly antipodal, continent-sized, low-velocity anomalies have been detected beneath Africa and the Pacific (e.g., Dziewonski, 1984; Hosseini et al., 2020; Ritsema et al., 2011; Simmons et al., 2010) that are known as Large-low velocity provinces (LLVPs). Although these regions have been widely studied, their origin currently remains unknown. These LLVPs are typically surrounded by fast seismic velocities that have long been interpreted as

Writing – original draft: Surya Pachhai
Writing – review & editing: Surya Pachhai, Michael S. Thorne, Sebastian Rost

remnants of ancient subduction (e.g., Grand, 2002; Grand et al., 1997; Sigloch, 2011). At the other end of the seismic spectrum studies find scatterers with sub-seismic wavelength scale lengths (on the order of 10's km) that may be related to the mixing and stirring of mantle materials throughout the Earth's history and are typically described statistically in terms of their correlation length and magnitude of velocity perturbation (e.g., Hedlin et al., 1997; Rost, Thorne, et al., 2006; Rost et al., 2015; Shearer, 2007). Between these extremes, at the medium and small length-scales (100–1,000 km), studies find heterogeneities below the resolution level of tomographic images that are nonetheless resolvable through detailed waveform and/or travel-time studies (e.g., Bréger & Romanowicz, 1998; Wysession et al., 1999). Here we focus on one of the most enigmatic of these features known as ultralow-velocity zones (ULVZs) located on top of the core-mantle boundary (CMB). ULVZs are defined as thin layers with a strong decrease in S-wave velocity (δV_s) of up to 50% (e.g., Havens & Revenaugh, 2001; Rondenay & Fischer, 2003), a strong decrease in P-wave velocity (δV_p) of up to 25% (e.g., Thybo et al., 2003) and an increase in density ($\delta\rho$) of up to 20% (e.g., Yu & Garnero, 2018) with respect to 1-D Earth reference models (e.g., Dziewonski & Anderson, 1981; Kennett et al., 1995). These structures may range in scale from a few 10s of km (e.g., Idehara, 2011; Rost & Revenaugh, 2004; Rost et al., 2005; Rost, Garnero, et al., 2006) to more than 1,000 km in lateral extent (e.g., Jenkins et al., 2021; Krier et al., 2021; Li et al., 2022; Thorne et al., 2021) and are typically only a few to 10s of km thick with thinner layers below the seismic resolution level being possible (Rost et al., 2010).

Since the first detection of ULVZs almost three decades ago (Garnero et al., 1993), more than 50 seismic studies have focused on the quantification of ULVZ parameters using an assortment of seismic probes (see recent review by Yu and Garnero (2018)) with approximately 25% of the studies using diffracted seismic phases ($SP_{diff}KS/SKP_{diff}S$, P_{diff} and S_{diff}), mainly by exploiting the $SP_{diff}KS$ seismic phase which consists of an SKS wave with a short segment of P-wave diffraction (P_{diff}) along the CMB (Choy, 1977; Garnero et al., 1993; Garnero & Helmberger, 1995). This phase provides constraints on both P- and S-wave velocity (e.g., Garnero & Helmberger, 1998) and provides large sampling coverage of the CMB (e.g., Thorne et al., 2020; Thorne et al., 2021; Thorne & Garnero, 2004). However, the location of ULVZs imaged with $SP_{diff}KS$ is ambiguous because of the existence of the complementary P_{diff} legs on the source- ($SP_{diff}KS$) and receiver-side ($SKP_{diff}S$). As a result, geometric arguments are typically employed to argue for ULVZ location (e.g., Thorne et al., 2019; Thorne et al., 2021). Other core-diffracted phases (e.g., S_{diff}—an S-wave diffracted along the mantle side of the CMB) have also been utilized to image large ULVZs (e.g., Cottaar et al., 2022; Cottaar & Romanowicz, 2012; Kim et al., 2020; Yuan & Romanowicz, 2017). As these diffracted waveforms are observed at longer periods (e.g., 5–10 s for $SP_{diff}KS$ and 10–20 s for S_{diff}), they are more sensitive to large-scale structures and cannot provide fine-scale ULVZ structures.

In contrast to diffracted waveforms, short period core-reflected waveforms such as ScP (Figure 1; e.g., Rost & Revenaugh, 2004; Rost et al., 2005; Rost, Garnero, et al., 2006) and PcP (e.g., Revenaugh & Meyer, 1997; Ross et al., 2004), and longer period ScS (e.g., Avants et al., 2006; He & Wen, 2009; Zhao et al., 2017) are used to image ULVZ structures at higher lateral (as short as ∼100 km) and vertical (as thin as 2-km thick, e.g., Rost et al., 2010; Pachhai et al., 2015; Pachhai, Li, et al., 2022) resolution. In the presence of a single-layer ULVZ, three additional phases are generated when considering the ScP arrival (Figures 1b and 1c; standard pre- and post-cursors for a 1D ULVZ). These are two primary conversions (i.e., SdP and SPcP, known as precursors) that arrive earlier than the main ScP phase and one phase that arrives later than ScP (ScsP, known as a postcursor). Among these conversions, the ScsP postcursor is the most prominent arrival and has an amplitude that is predicted above the noise level for many ULVZ models. Indeed, this post-cursor has been reported as a large dominant arrival in many ScP studies (e.g., Idehara, 2011; Idehara et al., 2007; Rost et al., 2005). However, the two pre-cursors are difficult to observe even for thick ULVZs (Figure 1) as their amplitudes are often below the noise level and/or obscured by the main ScP arrival for thin ULVZs and stacking of waveforms might be necessary to raise them above the noise level (e.g., Rawlinson & Kennett, 2004; Rost & Thomas, 2002). We note that measuring the timing and amplitude of the precursor arrivals offer the exciting possibility of being able to constrain ULVZ thickness, P-wave velocity, and density. As demonstrated in previous studies, the timing and amplitude of the ScsP postcursor provides good constraint on ULVZ S-wave velocity (e.g., Brown et al., 2015). As a result, S-wave velocity is well resolved while the P-wave velocity and density are weakly resolved (e.g., Pachhai, Li, et al., 2022) and their robust measurements are still challenging.

Resolving all the ULVZ parameters is essential to understanding the origin of ULVZ structures. The first ULVZ studies suggested that P-wave velocity decreases were as large as 10% (Williams & Garnero, 1996). In order to

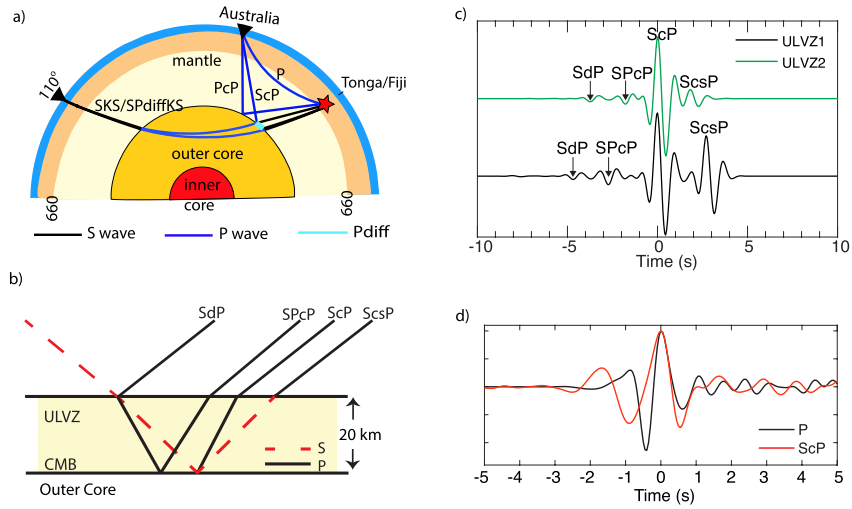

Figure 1. (a) Ray paths for direct P-wave, PcP wave, and ScP wave recorded at 40°, and SKS and $SP_{diff}KS$ at 110°. (b) Schematic diagram of 1-D Ultralow-velocity zone (ULVZ) precursors (SdP, SPcP) and postcursor (ScsP) relative to main ScP arrival. (c) Synthetic waveforms computed, using Wentzel, Kramers, Brillouin and Jeffreys at 40° epicentral distance, for a ULVZ with a strong (ULVZ1—black line) and weak (ULVZ2—green line) impedance contrast. ULVZ parameters for ULVZ1 are $h = 20$ km, $\delta V_p = -10\%$, $\delta V_s = -30\%$, and $\delta\rho = 10\%$ and for ULVZ2 are $h = 20$ km, $\delta V_p = -10\%$, $\delta V_s = -10\%$, and $\delta\rho = 5\%$. (d) Example stack of observed ScP (red) and P (black) waveforms that illustrate the pulse widths of P and ScP for a 298-km deep event on 27 July 2012 and recorded at Warramunga Array array.

explain these large velocity reductions, it was proposed that ULVZs may consist of partial melt with a prediction that this should entail a 3:1 ratio of S- to P-wave velocity perturbations (Berryman, 2000; Williams & Garnero, 1996). Such large S-wave velocity perturbations were at the time thought preposterous (Q. Williams, 2022, pers. comm.). However, subsequent studies have shown that ULVZ properties may be consistent with this 3:1 ratio (see e.g., Havens & Revenaugh, 2001; Revenaugh & Meyer, 1997). This interpretation is often cited for ULVZs that are located within the LLVP boundaries where higher temperatures could lead to partially molten mantle or LLVP material. However, not all ULVZs are found within LLVPs and may even be associated with high-velocity regions (e.g., Niu & Wen, 2001; Ross et al., 2004; Thorne et al., 2019; Thorne et al., 2021), where the temperature is assumed to be lower than that in the LLVPs. These ULVZs have been interpreted as the partial melt of mid-ocean ridge basalt (MORB) material in downwelling slabs (e.g., Andrault et al., 2014). But mechanisms besides partial melting such as iron-enrichment of (Mg, Fe)O can also explain an increase in density and a decrease in velocity observed in ULVZs (Wicks et al., 2010, 2017). Other compositional ULVZ origins have also been suggested such as iron-enriched post-perovskite (e.g., Mao et al., 2006), silicate sediment deposition on the top of the outer core (Buffett et al., 2000), subducted banded iron formations (Dobson & Brodholt, 2005), products of the chemical reaction between the silicate mantle and Fe-rich core (Mergner et al., 2021; Otsuka & Karato, 2012), and slab-derived materials (Hu et al., 2016; Liu et al., 2016). Other possible mechanisms include crystallization of basal magma ocean (e.g., Labrosse et al., 2007; Pachhai, Li, et al., 2022), and phase transition of minerals (e.g., Murakami et al., 2004; Shim et al., 2004). Currently, the physical origin of ULVZs is still poorly known, and a single mechanism may not explain all the observed ULVZs.

To improve our understanding of ULVZs' physical origin and their influence on mantle dynamics and core-mantle interactions, it is crucial to estimate ULVZ parameter (thickness—h, P-wave velocity reduction—δV_P, S-wave velocity reduction—δV_S, and density increase—$\delta\rho$) values as robustly as possible. However, inferred ULVZ properties may vary significantly within a small lateral extent of the CMB. For example, beneath the Coral Sea south of New Caledonia Island, Rost and Revenaugh (2003) suggest the presence of ULVZs with thickness ranging from 4 to 33 km, P-wave velocity reductions from −10% to 0%, S-wave velocity reductions from −30 to −10%, and density increases from 0% to 50%. Additionally, Rost and Revenaugh (2001) suggested the presence of zones with deposits of light core sediments (known as core rigidity zones) on the top of the liquid outer core and lack of ULVZs in the same study area. ULVZs in this region also appear intermittently (Rost & Revenaugh, 2001, 2003; Rost et al., 2005, 2010; Rost, Garnero, et al., 2006). The most recent study in this region further identifies multi-layer ULVZs with stronger decrease in S-wave velocity as a function of ULVZ depth (Pachhai, Li, et al., 2022).

The observed variation in resolved ULVZ parameters can be due to the several limitations in the estimation of these parameters that need to be addressed. The first limitation comes from non-uniqueness of ULVZ parameters due to nonlinearity and trade-offs in the model space (Garnero et al., 1998; Pachhai et al., 2014). Traditionally, ULVZ parameters are inferred mostly based on the observation of pre- and post-cursors of core-reflected and diffracted waveforms. However, identification of the additional pre- and post-cursors due to ULVZs is challenging, particularly when ULVZs have a weak impedance contrast (Figure 1). To address this challenge, we further develop and apply a fully non-linear waveform inversion of multiple events based on the Bayesian inversion approach that provides an ensemble of model solutions which contain all the models that explain the observed features in data (Pachhai et al., 2014, 2015; Pachhai, Li, et al., 2022). This approach provides ULVZ parameter values with their uncertainties by balancing the trade-off between misfit and model complexity. In this approach, ULVZ parameters are randomly perturbed from the reference model and waveforms are predicted for the perturbed model which is then compared with the observed waveforms. The perturbed model is accepted or rejected based on the improvement of fit between observed and predicted data. We update the perturbed model if the model is accepted. Otherwise, if the perturbed model were rejected, the reference model is retained and perturbed again. This process is repeated for more than 100,000 iterations and an ensemble of models that adequately fit the data is collected to infer the most likely model along with uncertainties. This approach allows us to see all the competing models including multi-modal solutions, where more than one unique model adequately explains the complexity in the data. Our full Bayesian inversion approach is outlined in Section 2.2.

The second limitation of traditional ULVZ modeling comes from the attenuation of seismic waves in the mantle and especially the differential attenuation between the core reflected phases (PcP/ScP/ScS) and a reference phase (typically P or S). In ScP studies, waveforms for the direct P-wave arrival are used as an approximation of the seismic source for comparison with waveforms for the ScP arrival. But, the two arrivals travel significantly different paths, particularly in the lower mantle (Figure 1a). Traditionally, the P-wavelet is convolved with synthetic spike trains to create synthetic ScP waveforms and then compared with the observed waveforms (e.g., Rost & Revenaugh, 2001, 2003). This approach works well when the pulse widths for the P- and S-waves are similar, which is not always the case due to the different attenuation along the P and ScP paths. Although most studies consider deep events and the strongest attenuation from the uppermost mantle is mostly avoided, the ScP pulse is still commonly broadened with respect to the direct P-wave (e.g., Figure 1d). This can be addressed by convolving the P-wavelet with an attenuation operator (i.e., t^* operator; Futterman, 1962) to approximate the differential attenuation between the arrivals. This is typically done by trial and error to find the t^* operator giving the most similar pulse width between P and ScP (e.g., Rost et al., 2005; Thorne et al., 2021). However, broadening of the ScP pulse width can also be due to thin and/or weak ULVZ structure. Therefore, an additional trade-off between attenuation in the lowermost mantle and ULVZ structure exist in the estimation of ULVZ parameters. To address this trade-off, we consider t^* as an additional unknown in the Bayesian inversion process and perturb it like other ULVZ parameters as described above.

The third limitation is due to the estimation of ULVZ parameters using waveforms from a single event. Stacked ScP waveforms for different events may not be similar due to both source side complexity (e.g., near source structural complexity such as slab structure or complex source-time function—STF) and the level of noise in the data. These additional complexities can get mapped into an inaccurate estimation of ULVZ parameters, particularly for P-wave velocity and density, which are constrained by the low amplitude pre-cursor arrivals, that is, by a top-side reflection (SdP) and a conversion (SPcP) from the ULVZ (Figures 1b and 1c). The amplitude of S-to-P transmission from the top of the ULVZ is roughly 10 times smaller than that of S-to-S, which ultimately results in the ScsP postcursor having a much larger amplitude than the two precursors (Figure 1c). Additionally, significant trade-offs exist between different ULVZ parameters (Figure S1 in Supporting Information S1), particularly between thickness and S-wave velocity perturbation (Figure S1b in Supporting Information S1), because a ULVZ with large height and weaker perturbation in S-wave velocity provides similar effects on the arrival time of the ScsP postcursor as a thinner ULVZ with a larger S-wave velocity perturbation. Additionally, there are trade-offs between density and P-wave velocity perturbations (Figure S1d in Supporting Information S1) as both parameters control the amplitude of the precursor while the trade-off between S-wave velocity and P-wave velocity (Figure S1f in Supporting Information S1) is due to their effect on the arrival time of the precursor (SPcP) relative to ScP. To address these challenges, we perform a joint inversion of ScP waveforms from multiple events. In this approach, a Green's function computed for ULVZ parameters is convolved with P-wavelets from multiple events which are then compared with the ScP wavelets for the corresponding events. As a result, the influence of extra

complexities, such as introduced by noise or local near-source structure, is reduced, thereby providing a more robust estimation of ULVZ parameters.

Regardless of the seismic phase used, it is exceptionally challenging to provide a robust estimate of ULVZ parameters from observed data due to the limitations summarized above. To address these challenges, we first perform a series of synthetic tests in order to determine how to best improve the Bayesian inversion process for ULVZ properties. Here we further develop the inversion method using ScP, which allows us to invert both path attenuation and ULVZ parameters simultaneously and perform an inversion of data from multiple events simultaneously. We then apply these new methods to analyze 291 events with high SNR recorded by the Warramunga and Alice Spring Arrays in Australia which sample the CMB beneath the Coral Sea (south of New Caledonia Island). Our joint Bayesian inversion of multiple events shows the Coral Sea region to contain complex ULVZ structures that appear thicker to the northeast than the southwest. The mean thickness in the northeast area is 14.8 km while that in the southwest area is 9.5 km. The S-wave velocities appear to be most robustly estimated, and its average $\sim -14\%$ across the entire study region, but the S-wave velocity in the northeast area decrease up to 21% while that in the southwest area decreases up to 37%. P-wave velocity reductions are typically smaller (on the order of -0 to -12%). The appearance of more than one ScP post-cursor in some of these data suggest possible 2-D or 3-D ULVZ structures may also exist within the region.

2. Data and Method

2.1. ScP Waveform Data

In this paper, we consider vertical component recordings for earthquakes occurring between 2005 and 2021 in the Tonga region and recorded by the seismic instruments in the Warramunga Array (WRA) and the Alice Spring Seismic Array (ASAR) in Australia's Northern Territory (Glanville & Geoscience Australia, 2011). ASAR has 19 short-period vertical-component stations with a narrow aperture of ~10 km, and WRA has 20 short-period vertical-component stations with an aperture of ~25 km. WRA is located approximately 400 km north of ASAR. The seismometers are identical within each array, so we do not remove the instrument response for the analysis. ASAR stations are distributed randomly with a roughly circular configuration while the WRA stations are distributed in an L-shape with additional stations near the corner of the L. Comparatively, the inter station spacing for the ASAR (~2 km) is shorter than that for the WRA array (~2.5 km).

We selected low magnitude events ($5.0 < mb < 6.0$) with depths greater than 100 km. Deep events are required to clearly separate the ScP and PcS arrivals without any interference. The epicentral distance between earthquakes in Tonga and WRA/ASAR array in Australia is ~40°, which is ideal for high signal-to-noise ratio (SNR) ScP waveforms. Our initial search provided us with 250 events for ASAR and 287 events for WRA. We bandpass filtered all seismic traces with corners at 0.5 and 1.5 Hz. Next, we manually inspected all the events and picked P and ScP arrival times. Any events with unusually complex P waveforms and/or ScP with poor SNR were discarded. Within the stations for each array we aligned waveforms separately for the P and ScP arrivals based on the 1-D prediction using the ak135 model (Kennett et al., 1995). Then both P and ScP waveforms for each event were aligned and stacked using the adaptive stacking approach (Rawlinson & Kennett, 2004), which improved the SNR of the traces. This approach minimizes the misfit between the stacked waveform and the individual waveforms in an iterative procedure to obtain the optimal alignment between traces. Then the waveforms for all the events were visually inspected again, and events with additional complexity in the P wavelet that we see as significant based on our synthetic experiments (presented in Section 3.2) were discarded from further analysis. This reduced the events down to 132 for ASAR and 159 for WRA. Figure 2 shows the station, event, and ScP bounce points at the CMB due to the events considered in this study. These data sample the CMB beneath the Coral Sea and south of New Caledonia Island. The ScP CMB bounce-points are grouped in two broad clusters (Figure 2). The largest cluster is in the southwestern part of our study region within a region of high probability of ULVZ occurrence obtained using $SP_{diff}KS$ (Thorne et al., 2021) while the smaller northeast area samples a region with very low probability of ULVZ occurrence. A portion of the southwest cluster has been previously studied using WRA (Pachhai, Li, et al., 2022; Rost et al., 2005) and ASAR (Brown et al., 2015; Rost, Garnero, et al., 2006) data independently.

2.2. Bayesian Inversion

To estimate the ULVZ elastic parameters (thickness, P- and S-wave velocity, and density) and ScP pulse attenuation (t^*) with their uncertainties, we expanded a Bayesian waveform inversion approach developed in Pachhai

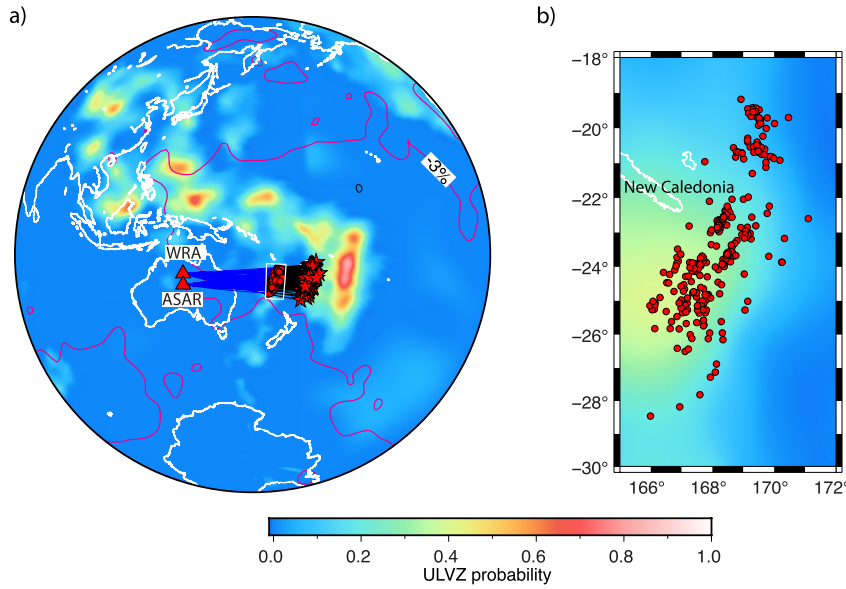

Figure 2. (a) Warramunga Array and Alice Spring Seismic Array array locations (red triangles), event locations (red stars), and ScP ray paths (blue lines for receiver side and black lines for source side) for events considered in this study. The background colors represent the probability of Ultralow-velocity zone occurrence (Thorne et al., 2021). The small white box indicates the detailed study area shown in panel (b). Red lines indicate the −3% contour line for S-wave velocity from tomography model S40RTS (Ritsema et al., 2011). (b) Red circles with black outline show the ScP bounce points on the core-mantle boundary for events used in this study.

et al. (2014) for simultaneous inversion of data from multiple events. In Bayesian inversion, the posterior probability density (PPD) represents the solution to an inverse problem which is expressed in terms of a conditional probability. Therefore, the PPD of a model vector ($\boldsymbol{m}$) given the data vector ($\boldsymbol{d}$) is represented by $p(\boldsymbol{m}|\boldsymbol{d})$, and the PPD combines the prior (independent of data) represented by $p(\boldsymbol{m})$ and likelihood (incorporates data information) represented by $p(\boldsymbol{d}|\boldsymbol{m})$ using Bayes' theorem as

$$p(\boldsymbol{m}|\boldsymbol{d}) = \frac{p(\boldsymbol{d}|\boldsymbol{m})p(\boldsymbol{m})}{\int p(\boldsymbol{d}|\boldsymbol{m})p(\boldsymbol{m})d\boldsymbol{m}}, \tag{1}$$

The integral term in the denominator represents a normalization constant and is also referred to as the evidence (i.e., data information that supports the chosen model), which is also known as the marginal likelihood. We note that the computation of evidence is challenging for nonlinear problems, but the evidence does not need to be computed for relative inference in a group of models as that term becomes a proportionality constant in Equation 1. In geophysical inversion data are fixed, therefore $p(\boldsymbol{d}|\boldsymbol{m})$ in Equation 1 becomes only a function of $\boldsymbol{m}$ and is represented by the likelihood $L(\boldsymbol{m})$. The likelihood function introduces data information to the inversion and quantifies the likelihood that a particular parameter vector gives rise to the observed data. The likelihood function must be derived from an assumption about the statistical distribution of the data errors. Note that data errors are generally not directly accessible in inverse problems and must be approximated by residual errors which combine both measurement (errors as a result of the measurement such as instrumental errors or environmental noise) and theory errors (errors resulting from approximations in the model including seismic wave propagation and/or prediction using a 1-D Earth model). Here, we assume Gaussian data errors. The likelihood for these errors for a single ScP waveform is expressed in the following form (Pachhai et al., 2014, 2015).

$$L(\boldsymbol{m}) = \frac{1}{|\boldsymbol{C}_d|}\exp\left[-|\boldsymbol{d}^{obs} - \boldsymbol{d}(\boldsymbol{m})|\frac{1}{\boldsymbol{C}_{d_i}}|\boldsymbol{d}^{obs} - \boldsymbol{d}(\boldsymbol{m})|\right], \tag{2}$$

where $\boldsymbol{C}_d$ is the noise covariance matrix that incorporates both correlated and uncorrelated noise. Here our goal is to invert for multiple events simultaneously, therefore, this expression can be readily modified for the joint inversion as:

$$L(\boldsymbol{m}) = \prod_{i=1}^{N}\frac{1}{|\boldsymbol{C}_{d_i}|}\exp\left[-|\boldsymbol{d}_i^{obs} - \boldsymbol{d}_i(\boldsymbol{m})|\frac{1}{\boldsymbol{C}_{d_i}}|\boldsymbol{d}_i^{obs} - \boldsymbol{d}_i(\boldsymbol{m})|\right], \tag{3}$$

where, N is the total number of waveforms (i.e., number of events) considered in the inversion. In a previous study (Pachhai et al., 2014), the model vector ($\boldsymbol{m}$) contained only ULVZ properties: layer thickness, P-wave and S-wave velocity, and density perturbations. Here, the model vector also includes the ScP pulse attenuation parameter as t^* also becomes an unknown in the inversion.

The correlated errors are considered in the inversion by applying an autoregressive process of order 1 (AR1), the details of which are provided in Dettmer et al. (2012). In this case, the likelihood function can be formulated as

$$L(\boldsymbol{m}) = \prod_{i}^{N} \frac{1}{\sigma^{npts_i}\sqrt{(2\pi)^{npts_i}}} \exp\left[\frac{1}{2\sigma_i^2}\left|\left(\boldsymbol{d}_i^{obs} - \boldsymbol{d}_i(\boldsymbol{m}) - \boldsymbol{d}_i(a_i)\right)\right|^2\right], \tag{4}$$

where $npts$ is the number of data points in a single waveform, $\boldsymbol{d}(a)$ are AR1 predictions for AR1 parameters a, which accounts for serial correlation. In the AR1 model, a time series (i.e., data noise in this case) at time t is predicted by the product of the AR1 coefficient (a in Equation 4) and time series at time $t-1$ plus the random noise defined by the standard deviation (σ in Equation 4). Here, the standard deviation of the residual errors (σ) and the AR1 coefficient are treated as unknowns, and $\boldsymbol{d}(\boldsymbol{m})$ is the predicted data. We compute the Green's functions using the Wentzel, Kramers, Brillouin and Jeffreys (WKBJ) method (Chapman & Orcutt, 1985) assuming a flat and 1-D ULVZ layer on the top of the CMB. Then the synthetic predictions are obtained by convolving the source time function (STF) with the Green's functions (i.e., $\boldsymbol{d}_i(\boldsymbol{m}) = \boldsymbol{G}_i(\boldsymbol{m})$ * STF_i). Here we use the stack of P waveforms at each array to obtain the empirical STF for each event.

Inversion of seismic waveforms is a non-linear problem and a solution to the inverse problem is approximated by the PPD, which provides parameter estimates and uncertainties by marginalization. However, there exist no analytical solutions for the PPD, therefore, a numerical sampling algorithm is considered to estimate the PPD numerically. The sampling algorithm can be inefficient for highly non-linear problems, particularly when high probability regions are separated by a low probability region. In that case, sampling algorithms such as Markov Chain Monte Carlo (MCMC) may have difficulty in converging on the global minima. Here, we apply interacting MCMC, also known as parallel tempering, to overcome this problem. In this algorithm, a model is randomly proposed from a uniform prior in each iteration. Then the proposed model is accepted or rejected with probability (α). If $q(\boldsymbol{m}', \boldsymbol{m})$ is the distribution for a proposed transition from the current model ($\boldsymbol{m}$) to a new model ($\boldsymbol{m}'$), the proposed model is then accepted or rejected using the following probability.

$$\alpha = \min\left[1, \frac{p(\boldsymbol{m}')}{p(\boldsymbol{m})}\left(\frac{L(\boldsymbol{m}')}{L(\boldsymbol{m})}\right)^{\beta}\frac{q(\boldsymbol{m}, \boldsymbol{m}')}{q(\boldsymbol{m}', \boldsymbol{m})}\right], \tag{5}$$

where β is the tempering parameter used for parallel tempering and is the reciprocal of the temperature width (dT). In Equation 5, the priors do not change, that is, $p(\boldsymbol{m}') = p(\boldsymbol{m})$, and proposals ($q(\boldsymbol{m}, \boldsymbol{m}')$, and $q(\boldsymbol{m}', \boldsymbol{m})$) are symmetric, therefore, the acceptance/rejection probability is given by the β power of the likelihood ratio (i.e., $\left(\frac{L(\boldsymbol{m}')}{L(\boldsymbol{m})}\right)^{\beta}$).

In parallel tempering, lower values of β decrease the likelihood function in Equation 2 resulting in wider exploration of the parameter space while chains with high β-values preferentially sample high posterior probability regions. Parameter inferences are made based on a chain with $\beta = 1$ that provides unbiased samples from the PPD. The MCMC sampling is performed in several chains with different β-values. After performing MCMC sampling within-chain, parameters from randomly selected chain pairs are proposed to swap/exchange between chain pairs. For example, suppose $\boldsymbol{m}_t^i$ are the parameters of the chain i and $\boldsymbol{m}_t^j$ are the parameters of the chain j at tth iteration. Then parameter swap between two chains i and j is proposed which is accepted or rejected based on the Metropolis Hasting acceptance probability (α_β, Gilks & Roberts, 1996) defined by;

$$\alpha_\beta = \min\left(1, \frac{p_i\left(\boldsymbol{m}_t^j\right)p_j\left(\boldsymbol{m}_t^i\right)}{p_i\left(\boldsymbol{m}_t^i\right)p_j\left(\boldsymbol{m}_t^j\right)}\right), \tag{6}$$

where $p_i(\boldsymbol{m})$ is tempered target distribution given by, $p_i(\boldsymbol{m}) = [p(\boldsymbol{m})]^{\beta_i}$.

If the proposed swap is accepted, parameters are exchanged and updated to proceed for the next iteration. In contrast, if the proposed swap is rejected, parameters are retained in both chains. Then the sampling is moved

for the next iteration. This procedure allows the algorithm to take advantage of the various ranges of exploration scales without biasing the PPD.

3. Synthetic Experiments

This section presents a series of experiments we performed which aim to address existing limitations on the robust estimation of ULVZ parameters. To best assess the biases encountered under a variety of situations, we implement Bayesian inversion of a single-layer ULVZ.

For all of the inversions presented in this section, we chose uniform priors from 0 to 50 km for ULVZ height (h), −50% to 0% for P-wave velocity (δV_P), −50% to 0% for S-wave velocity (δV_S), and 0%–30% for density ($\delta\rho$) with respect to the ak135 model (Kennett et al., 1995). The uniform prior bounds assigned for ULVZ parameters allows to identify non-ULVZ like structure as well. For example, if the ScP waves do not interact with the ULVZ, the perturbation values for δV_P, δV_S, and $\delta\rho$ become close to zero with no constraint on h. The prior for uncorrelated data noise (i.e., σ) is set from 0.0 to 0.2 (i.e., 20%), and the prior for the AR1 coefficients ($\boldsymbol{a}$) is set from 0 to 0.99. Data noise with $a = 0$ indicates no correlation between noise points while the data noise with $a = 1.0$ indicates perfect correlation. The prior range for t^* is 0.0–2.0. For parallel tempering (i.e., interacting MCMC), the number of chains required for efficient convergence highly depends on the problem, and we found that 12–16 chains are optimal to achieve faster convergence of the ULVZ parameters. All model parameters including the t^* values are proposed simultaneously with equal probability from the range given by the priors. After running more than 100, 000 iterations, the first third of the ensemble solutions are discarded as burn-in (ensuring that the sampling is not biased by the starting model). Samples after the burn-in period are considered for parameter inference. We monitor the convergence of the algorithm by examining the sampling history for various parameters by comparing inferences for the first third of PPD samples (post-burn-in period) to inferences for the last third. When no significant differences exist in the marginals of parameters, the sampling is considered to have converged.

3.1. Effect of Attenuation (t^*) Parameter in the Inversion of ULVZ

Studies using the ScP seismic phase typically use the P waveform as an approximation for the STF. However, the direct P-wave travels a shorter and different path than ScP (Figure 1a). Additionally, the ScP wave is expected to attenuate differently from that for the direct P-wave due to the starting S-leg of ScP. Therefore, the ScP pulse width can be broadened due to attenuation, particularly if ScP passes through a low-velocity zone. This can affect what ULVZ parameters are retrieved in the inversion. For example, if the ScP pulse is significantly broader than the P-wave pulse then ULVZ structure may be inferred in order to broaden the predicted ScP pulse. But this could be erroneous as attenuation may also play a role in broadening the ScP pulse. Previous studies have accounted for this by applying multiple t^* operators to the P-wavelet and visually determining the best-fit t^* value (Hansen et al., 2020; Rost et al., 2005, 2010; Thorne et al., 2021) assuming that the ScP pulse broadening is due to attenuation. However, this can also be erroneous if the broadening of the ScP pulse is in part due to the ULVZ structure rather than just attenuation. Example P and ScP wavelets are shown in Figure 1d. The wider pulse width for the ScP waveform in comparison to that for P can be either due to ULVZ or attenuation.

Here we address this trade-off between ULVZ parameters and attenuation by including a t^* value as a model parameter in the inversion. The attenuation parameter is defined by a t^* operator (e.g., Aki & Richards, 2002; Futterman, 1962; Rost et al., 2005). The higher value of t^* represents stronger attenuation (Shearer, 2019). To better understand the resultant t^* value for a realistic quality factor (Q) value of the 1-D Earth model, we computed synthetic seismograms for P and ScP for a Qs (attenuation of S wave) value of 500 everywhere in the mantle (Figure S2a in Supporting Information S1) which is on the order of realistic Earth model and a higher Qs value of 1,000 (Figure S2d in Supporting Information S1), which corresponds to less attenuation, using the reflectivity method (Müller, 1985). The estimation of t^* values for these attenuation models are shown in Figures S2b and S2c in Supporting Information S1. To compare t^* estimates, different values of t^* parameter are convolved with the P waveform and then the L2-norm misfit is measured to identify the best value of the t^* parameter. We found that the best-fitting t^* value for the model of quality factor $Q = 500$ is ∼0.6 while the one with $Q = 1{,}000$ has a t^* value ∼0.3. In this section, we present results for synthetic tests that include simultaneous inversion of both ULVZ and attenuation parameters for four different cases that span the end member scenarios that could be

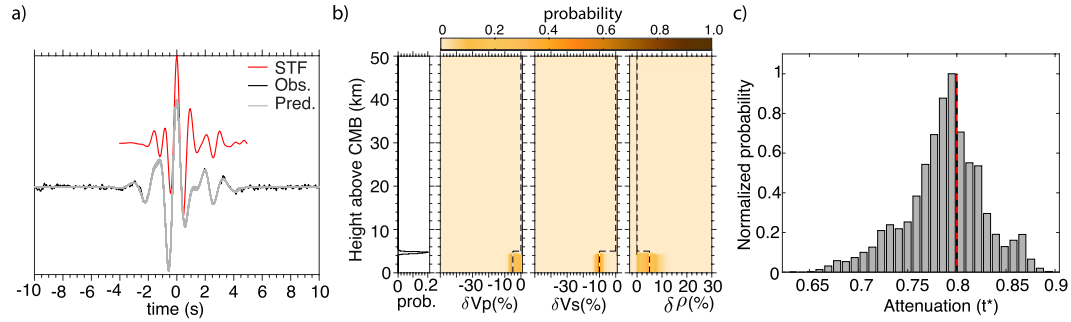

Figure 3. (a) Synthetic ScP waveform, generated for 5-km thick Ultralow-velocity zone (ULVZ) with a decrease in P velocity ($\delta V_P = -5\%$), a decrease in S-wave velocity ($\delta V_S = -10\%$), and an increase in density ($\delta\rho = -5\%$), with added noise (black line), constructed by attenuating the source time function (red line) with a t^* value of 0.8. The gray lines represent the predictions for 100 randomly selected models from the posterior distribution. (b) Inversion results for interface probability, P-wave velocity perturbation (δV_p), S-velocity perturbation (δV_s), and density perturbation ($\delta\rho$) as a function of ULVZ height (h) above the core-mantle boundary. The darker color represents a higher probability while the lighter color represents a lower probability. (c) Posterior probability density of the t^* parameter. The dashed lines in (b) and (c) represent the true values used to prepare the synthetic ScP waveform.

encountered in real data. These cases are, (a) we computed the Green's function for an ScP waveform that samples a 5-km thick ULVZ with a $\delta V_S = -10\%$, a $\delta V_P = -5\%$, and a $\delta\rho = +5\%$. Then we attenuated the P-wavelet using $t^* = 0.1$ and convolved it with the Green's function to predict the ScP waveform. This scenario represents a case where the ScP wavelet is weakly attenuated relative to the P-wavelet used as the STF. Because the attenuation applied is relatively weak, the pulse widths are similar for both ScP and P waveforms (Figure 3a). (b) In the second scenario, we considered the same attenuation parameter ($t^* = 0.1$) but for a ULVZ model with larger thickness and velocity perturbations. Here we used $h = 20$ km, $\delta V_S = -30\%$, $\delta V_P = -10\%$, and $\delta\rho = +10\%$. We consider this as a strong ULVZ. (c) In the third case, we considered the weak ULVZ of case 1, but this time we considered stronger attenuation with $t^* = 0.8$. This scenario assumes that the ScP wavelet is strongly attenuated relative to the P-wavelet. (d) In the fourth case, we used the strong attenuation ($t^* = 0.8$) and the strong ULVZ model of case 2. Finally, correlated noise generated using the first-order autoregressive (AR1) model (Dettmer & Dosso, 2012; Pachhai et al., 2014, 2015) was added to all the synthetic predictions. Seismic waveforms are shown for case 1 (weak ULVZ and strong t^*) in Figure 3a. We retrieved the ULVZ parameters and t^* value considering them as unknowns in the inversion with final inversion results shown in Figures 3b and 3c. The PPD for ULVZ parameters are shown in panel b, demonstrating that the inversion recovers ULVZ parameters well, and we show the histogram for t^* in panel c, showing a clear peak near the actual $t^* = 0.8$ value. The inversion results for all four cases described above are compared in Figure 4-d. These results indicate that all the ULVZ parameters including height and t^* values are recovered in all cases, but the uncertainties are different. Specifically, the uncertainties are higher for weaker ULVZ models (case 1 and 3 shown in Figures 4a–4c). This is because several other models with ULVZ parameters close to the true values provide a similar fit to the data.

For comparison, we ran the inversion for the same four cases described above, but this time we did not sample the attenuation parameter (t^* value). The inversion results for all four cases are shown in Figures 5a–5d. The inversion results indicate that all of the ULVZ parameters are recovered for case 2 with a strong ULVZ model and weak attenuation (Figure 5b). We start to see deviation between the recovered and input models for a weak ULVZ model with weak attenuation (case 1, Figure 5a) but the difference is not yet that large. In contrast, the inversions cannot recover any ULVZ parameters when the attenuation is large (i.e., $t^* = 0.8$, case 3 and 4, Figures 5c and 5d). This illustrates the importance of considering t^* in the inversion. If there is a substantial effect of attenuation in the observed ScP waveforms, the parameters retrieved without sampling t^* can be incorrect.

To understand the trade-off between ULVZ and attenuation parameters, we computed the joint marginal probability distributions for case 3 (Figure S3 in Supporting Information S1). In this case the ULVZ and attenuation parameters show strong trade-offs except for layer thickness and attenuation (t^*). The trade-off between S-wave velocity perturbation and t^* (Figure S3c in Supporting Information S1) is due to the fact that both weaker δV_s and higher values of t^* operator broadens the ScP pulse. On the other hand, the trade-offs between P-wave velocity perturbation and t^* (Figure S3b in Supporting Information S1), and between density perturbation and t^*

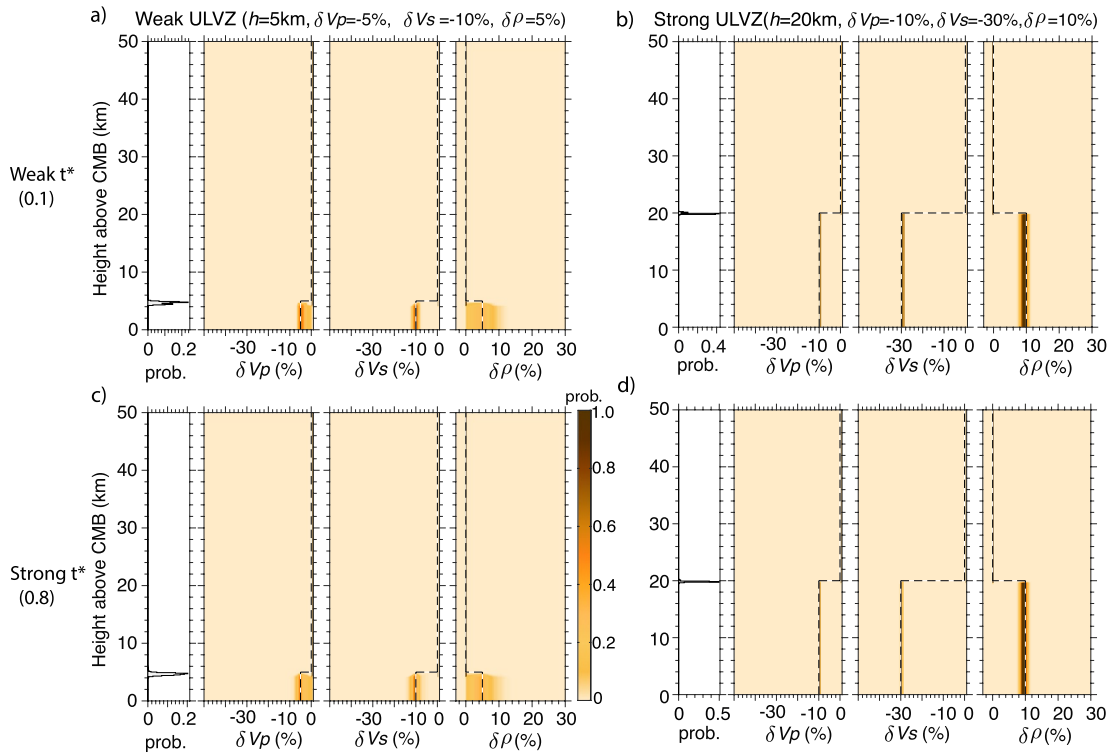

Figure 4. Inversion results for interface probability, δV_p, δV_s, and $\delta\rho$ as a function of Ultralow-velocity zone (ULVZ) height above the core-mantle boundary when t^* is also sampled in the inversion. Results for (a) Case 1: a weak ULVZ and a weak t^*, (b) Case 2: a strong ULVZ and a weak t^*, (c) Case 3: a weak ULVZ and a strong t^*, and (d) Case 4: a strong ULVZ and a strong t^*. The darker color represents a higher probability while the lighter color represents a lower probability. The dashed lines represent the true values used to prepare the synthetic ScP waveforms.

parameter (Figure S3d in Supporting Information S1) exist because all of these parameters change the amplitude of the precursors.

We note that the trade-offs between t^* and ULVZ parameters are not observed in the case when the ULVZ is strong and thick because the ScP post-cursor for thick and strong ULVZ does not interfere with the ScP pulse width.

3.2. Effect of Source Complexity in the Inversion of ULVZ

Using the P wavelet as a STF works well as long as it is impulsive with no additional complexities (Pachhai, Li, et al., 2022). However, this significantly limits how much data can be used in ULVZ studies as the P-wavelets can be complicated and, in some instances, appear more complicated than the ScP waveforms themselves. Therefore, it is of interest as to how much deviation from a single impulsive P-wavelet is acceptable in inverting for ULVZ structure. In this section we examine the effects of using P wavelets with various levels of complexities to understand their bias on the estimation of ULVZ parameters.

For the first set of experiments, we generate a synthetic ScP wavelet by convolving an attenuated P wavelet ($t^* = 0.8$) with the synthetic ScP Green's function for a ULVZ model with $h = 20$ km, $\delta V_S = -30\%$, $\delta V_P = -10\%$, and $\delta\rho = +10\%$. Then the observed noise obtained was added to the synthetic ScP wavelet. This synthetic prediction (shown in Figure S4a in Supporting Information S1) was used as the observation for our tests on STF complexity. The inversions were then applied using STFs with added complexity. To prepare these more complex STFs, we started with the original P wavelet (Figure S4b in Supporting Information S1) and convolved it with a spike train that has two delta functions. Figure S4c in Supporting Information S1 shows an example where the second delta function is delayed by 5 s and has an amplitude of 0.2 with respect to the first wavelet. The convolved STF with additional complexity for this example is shown in Figure S4d in Supporting Information S1. For our inversion tests, the amplitude of the second delta function was varied from 0.1 to 0.5 in increments of 0.1 (relative

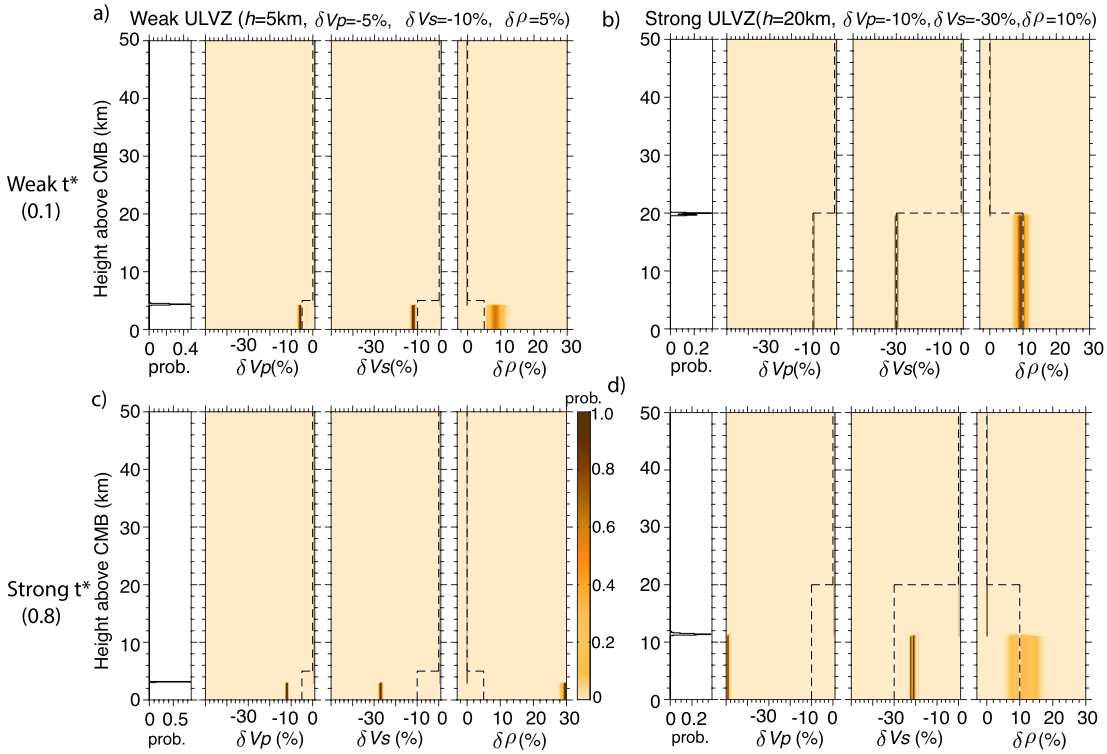

Figure 5. Inversion results for interface probability, δV_p, δV_s, and $\delta\rho$ as a function of Ultralow-velocity zone (ULVZ) height above the core-mantle boundary when t^* is not sampled in the inversion. Results for (a) Case 1: a weak ULVZ and a weak t^*, (b) Case 2: a strong ULVZ and a weak t^*, (c) Case 3: a weak ULVZ and a strong t^*, and (d) Case 4: a strong ULVZ and a strong t^*. The darker color represents a higher probability while the lighter color represents a lower probability. The dashed lines represent the true values used to prepare the synthetic ScP waveform.

to the normalized ScP amplitude) while the delay time of the second delta function was allowed to change from 0.25 to 5.0 s in increments of 0.25 s. Then the inversions were computed individually for all these STFs with and without including t^* in the inversion.

The inversion results with and without sampling the t^* parameter are shown in Figure 6. Note that in Figure 6, we saturate the color scale to gray in a region ±10% around the actual ULVZ parameter in order to highlight areas with reasonable agreement. For example, our original ULVZ model has a thickness of 20 km, and we consider that if our inversion result is within 10% of that value (i.e., between 18 and 22 km) the inversion performed sufficiently. Figure 6 shows that the inversion cannot retrieve any ULVZ parameters for most of the source complexities examined if the inversion is performed without sampling the t^* parameter. In this case, the ULVZ thickness recovered by the inversion is always much thinner than the true thickness (20 km) of the ULVZ while the S-wave velocity decrease is also larger than the true S-wave velocity (−30%). In contrast, when the inversion includes t^* as an unknown, ULVZ parameters are well retrieved within 10% from the true value of the ULVZ parameters for most of the amplitude and time delay of the second delta function. In particular, the inversion breaks down when the delay time of the second delta function (t_d) matches with the arrival time of the ScsP postcursor (note in Figure S4a in Supporting Information S1 the ScsP postcursor arrives 2.75 s after ScP). This mismatch is most evident for the largest amplitudes of the second delta function. Even if the ULVZ parameters are strong, the complexity in the STF can affect the retrieved ULVZ parameters. However, this primarily occurs when the amplitude of the second delta function relative to the main pulse is large. When the amplitude of the added complexity is lower than ∼20% of the main pulse all ULVZ parameters are well recovered.

We repeated the above experiments for two additional ULVZ models. First, for a ULVZ model with $h = 10$ km, $\delta V_S = -20\%$, $\delta V_P = -5\%$, and $\delta\rho = +10\%$, and second, a ULVZ model with $h = 5$ km, $\delta V_S = -25\%$, $\delta V_P = -5\%$, and $\delta\rho = +5\%$. Inversion results for these two models are shown in Figure S5 in Supporting Information S1, where we only show results for the case when inversions include t^* in the inversion. In these two cases, the ULVZ model is first weaker and then thinner than the first case presented. Both of these additional cases are more problematic

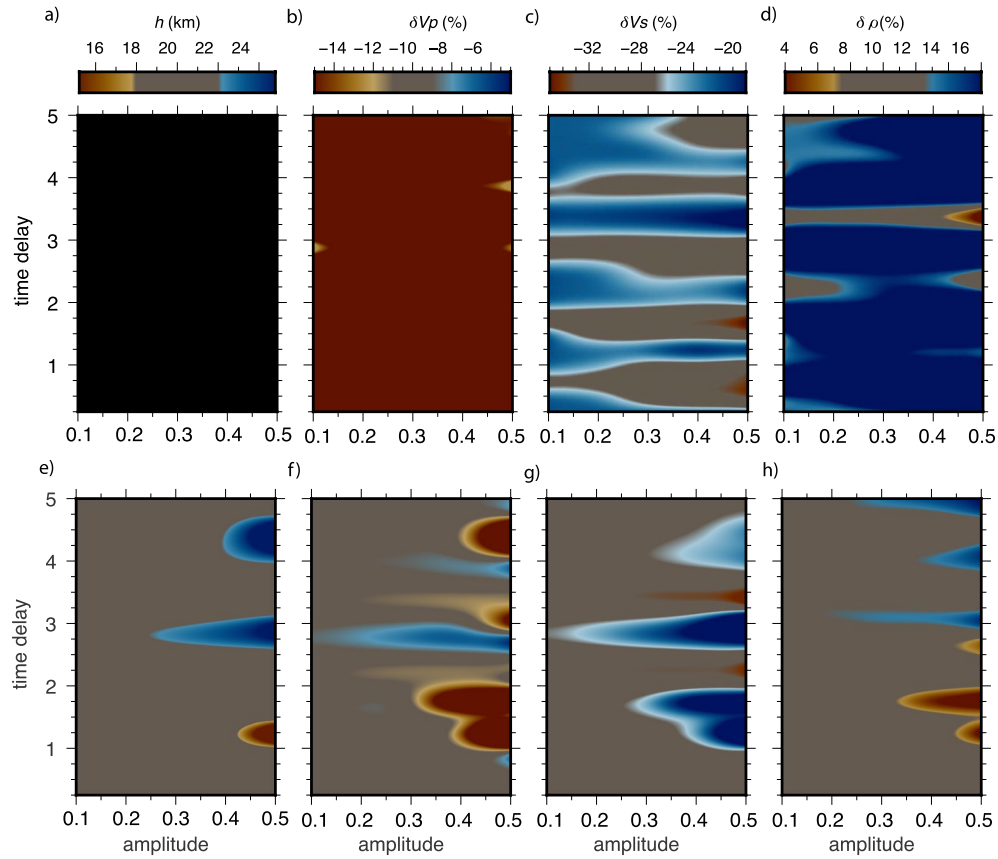

Figure 6. Inversion results using STFs with added complexity. Panels (a–d) show inversion results without sampling t^* parameter in the inversion and panels (e–h) show inversion results when sampling t^* parameter in the inversion. Inverted parameters are shown as a function of delay time and amplitude of the second pulse in the spike train. Parameters considered are (a, e) Ultralow-velocity zone thickness (h) (b, f) P-wave velocity reduction (δV_P) (c, g) S-wave velocity reduction (δV_S), and (d, h) density perturbation ($\delta\rho$).

for recovering ULVZ parameters in our inversion. As also discussed in Section 3.1, it is more difficult to recover ULVZ parameters from weaker and thinner ULVZ models because the amplitudes of pre- and post-cursor arrivals are lower. As shown in Figure S5 in Supporting Information S1, all ULVZ parameters, with the exception of thickness, are not recovered within 10% of the real value for a large portion of the model space explored.

Because of the challenges associated with recovering ULVZ parameters for weaker ULVZs when even moderate STF complexity exists, we sought to improve upon the characterization by jointly inverting multiple events at the same time. As a first test, we jointly inverted waveforms for the strong ULVZ model where for the first observation we used the worst-case scenario synthetic (here we used the second delta function at ∼2.5 s and then for the second observation we varied the second delta function as before). Inversion results for this case are shown in Figure S6 in Supporting Information S1. This shows that almost all ULVZ parameters retrieved from the inversions are incorrect.

For the second test, we considered synthetic predictions computed for the strong ULVZ model (see Section 3.2). In these inversions, we used STFs with varying amplitude and delay time of the second pulse as shown in Figures S4c and S4d in Supporting Information S1 (i.e., amplitude of the second pulse varied from 0.1 to 0.5 in the interval of 0.1 and delay time vary from 0.25 to 4.75 s in the interval of 0.75 s). The inversion was performed jointly for 2 to 5 events with varying complexities in the STFs. Note that the same synthetic prediction was replicated for multiple events. That means no complexities in the STFs used in the inversion were present in the synthetics with noise considered as data in the inversion. The inversion results for various STF complexities are shown in Figure 7. In this figure we only plot the maximum likelihood model. Figure 7 indicates that the recovered S-wave velocity reduction is close to the true ULVZ model while P-wave velocity and density perturbations deviate more

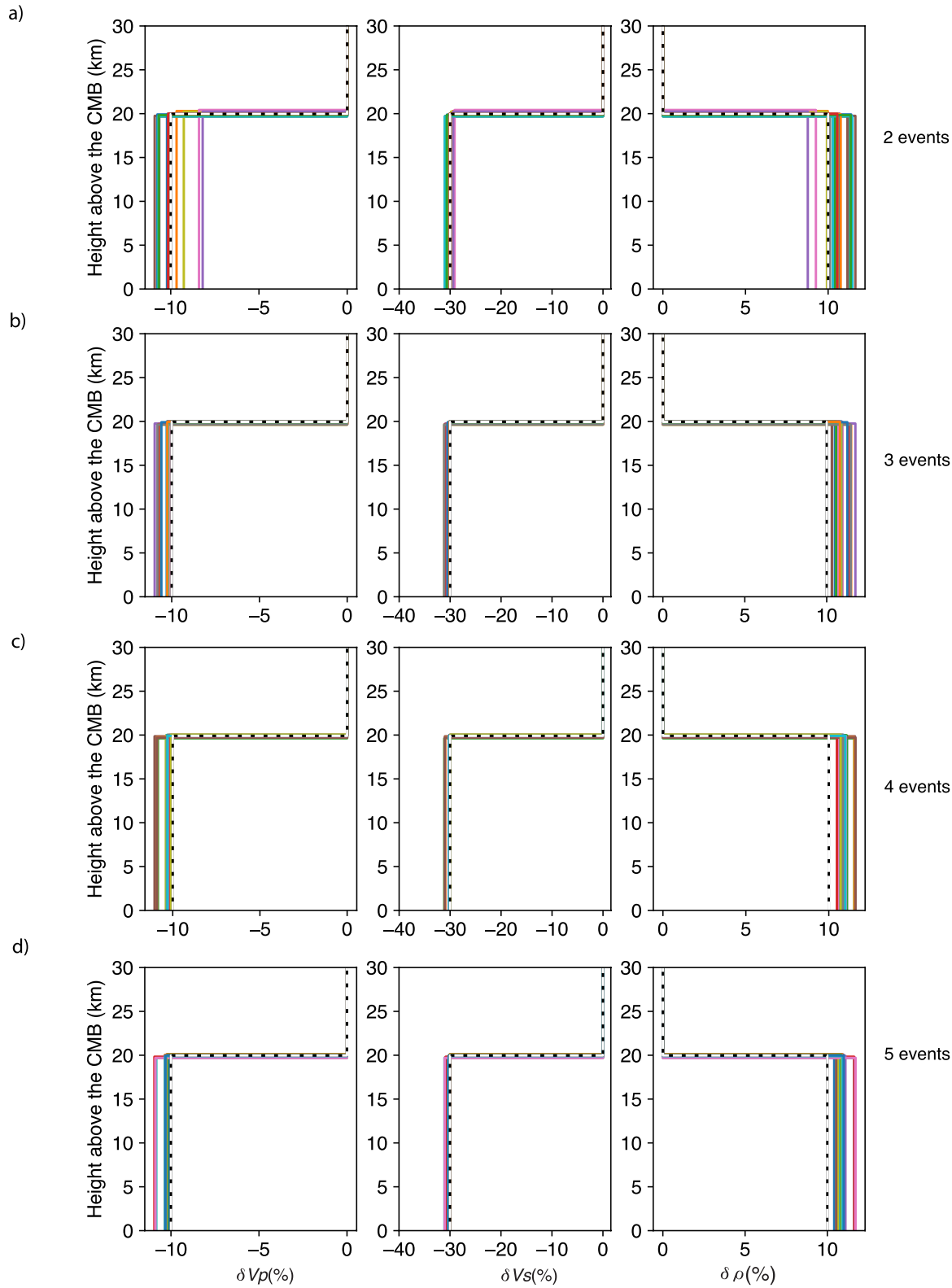

Figure 7. Maximum likelihood models recovered (color solid lines) for P-wave velocity reduction (δV_P), S-wave velocity reduction (δV_S), and density perturbation ($\delta\rho$) when (a) two, (b) three, (c) four, and (d) five events are considered in the inversion. The true models are indicated by dashed black and white lines.

from the true model (represented by black and white dashed lines) when two events are utilized in the inversion. The joint inversion of increased number of events shows that the recovered models are closer to the true ULVZ model. The results of this test suggest that when a larger number of events are used in the inversion, the inversion focuses on the coherent energy, for example, pre- and post-cursor arrivals, and noise is influencing the results less. The additional arrivals generated by the complexity of the STFs. The joint inversion of multiple events with complex STFs treats the additional arrivals of the different STF as noise, and inversions recover true structure when enough events are simultaneously included in the inversion.

These experiments illustrate that ULVZ parameters can be recovered, particularly for thickness and S-wave velocity perturbation as long as the amplitude of the second delta function is lower than ∼20% of the main pulse except for the cases where time delay for the postcursor and the second delta function are the same. Addition of complex STF influences the retrieval of the ULVZ parameter unfavorably. However, such influence can be minimized when enough events are inverted jointly.

3.3. Effect of Noise in the Inversion of ULVZ Parameters

An additional challenge in inverting for ULVZ parameters is the effect of noise. Although noise parameters are also included in the inversion as free parameters, sometimes large noise arrivals exist in the data and the inversion scheme attempts to fit those arrivals with ULVZ structure. To test the effect of noise in the inversion, we added random noise to our synthetics where we could control the noise characteristics. We generated random noise by convolving a Gaussian auto-correlation function (ACF) with a series of random numbers similar to that in Pachhai, Thorne, et al. (2022). Here we define the Gaussian ACF as:

$$\mathrm{ACF}(t) = \sigma e^{-t^2/T_{\mathrm{corner}}^2}, \tag{7}$$

where T_{corner} is the corner period, and σ is the root-mean-square (RMS) of the noise. We vary the RMS values from 0.1 to 0.5 with an interval of 0.1 and corner period from 0.5 to 5 s with an interval of 0.5 s. Noise was then added to a synthetic seismogram computed for a ULVZ model with $h = 20$ km, $\delta V_S = -30\%$, $\delta V_P = -10\%$, and $\delta\rho = +10\%$. These synthetics were then filtered in a 0.5–1.5 Hz frequency band that is typically used to analyze real data.

We added noise to our synthetic prediction for two different realizations of noise for a given RMS amplitude and corner period. First, the inversions were performed separately for the different noise realizations and then we jointly inverted both realizations simultaneously. The inversion results for the individual realizations are shown in Figures S7a–S7h in Supporting Information S1 and indicate that ULVZ parameters are retrieved well except in the case of extremely high frequency (i.e., short periods). However, the joint inversion of data using two noise realizations shows significant improvement in recovery of all the ULVZ parameters regardless of corner frequency and RMS amplitudes (Figures S7i–S7l in Supporting Information S1). Thus, joint inversion of multiple events appears to adequately handle possible overfitting of noise.

4. Results for Observed Data

4.1. Inversion Set-Up

We estimated ULVZ parameters applying Bayesian inversion of ScP data collected as described in Section 2.1 with ScP bounce points at the CMB beneath the Coral Sea. We conducted three separate inversion tests. In the first test, we inverted data from each event individually and did not group events into geographic bins. However, our synthetic experiments showed that inversion of individual events can provide meaningless results, particularly when the data exhibit coherent noise and/or the STF is complex (Figures 6 and 7; Figures S3 and S4 in Supporting Information S1). In our second and third tests we grouped data based on the geographic bins sorted by the ScP bounce points at the CMB. In both of these tests we simultaneously inverted for ULVZ parameters using multiple events sampling the same region of the CMB. Initially we grouped ScP bounce points by geographic bins with a radius of 1° on the CMB consistent with the approximate size of the ScP Fresnel zone (for ScP at 1 Hz the Fresnel zone is ∼120 km). However, visual inspection of the ScP waveforms showed significant variation within some of the bins. Therefore, we divided our study area into smaller geographic bins with a 0.5° radius and a 0.5° of overlap between bins. We only considered bins with at least 5 events (based on our synthetic experiments

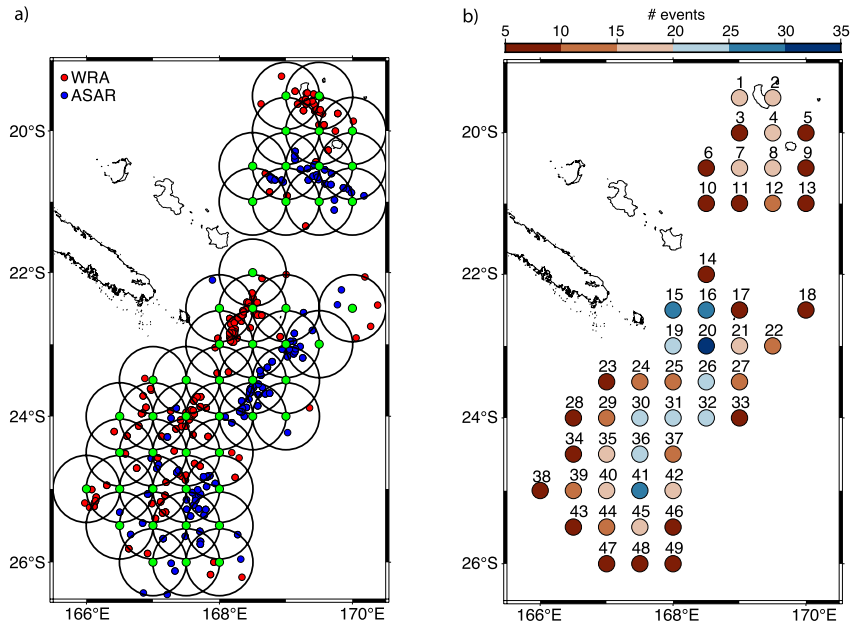

Figure 8. (a) Black circles show the 0.5° geographic bins used in this study. The green circles show the bin centers. ScP bounce points on the core-mantle boundary for events recorded at Warramunga Array are shown as red circles and for events recorded by Alice Spring Seismic Array are shown as blue circles. (b) Geographical map for the numbered bin centers. Circle color represents the number of events in each geographic bin. Bins are numbered as described in the text.

presented in Section 3.2) which gave us 49 total bins. The final distribution of geographical bins is shown in Figure 8. The number of events within each bin varies from 5 to 35. These two joint inversion tests differ based on how we consider t^* parameters as described in Sections 4.3 and 4.4.

As described above, the WKBJ Green's functions are convolved with the STF to make our forward prediction. Here we chose a 10 s time window for STF which contains a wide time window around the P-wavelet. We also selected events based on the complexity in STFs as suggested by our synthetic experiments. If the STFs were extremely complex with a ringing appearance or with additional high amplitude energy behind the direct P wave, we discarded those events. Figures 9a, 10a and 11a show example P and ScP waveforms for three geographic bins used in this study (bins 24, 37, and 41). We note that bins 37 and 41 are located within a degree of each other, but there are noticeable variations in waveforms between these two bins. In particular, there appear to be low amplitude pre- and post-cursors in the ScP waveforms that do not exist in the P-wavelet in the case of bins 24 and 37. In contrast, the P-wavelet appears to explain most of the features in the ScP waveforms in the case of bin 41 (Figure 11a). In bin 41, we also see that, in some cases, the P wavelet is more complex than that of ScP (e.g., event numbers 11, 16, 20, and 25). Nonetheless, we see from these examples that the P-wavelets are similar in appearance to the ScP waveforms in dominant period and do not contain significant complexities.

To perform the Bayesian inversion, we selected the time window to compare predictions for ULVZ models with the observed data based on the arrival time of pre- and post-cursors for ULVZs at the boundaries of our priors (δV_S and $\delta V_P = -50\%$, $\delta\rho = 30\%$, and $h = 30$ km). For a single layer 1-D model, the ScsP postcursor arrives 4 s after the main ScP phase when $\delta V_S = -45\%$ and $h = 20$ km. Similarly, the SdP precursor arrives 10 s before the ScP arrival when $\delta V_P = -45\%$ and $h = 30$ km. Therefore, we selected a time window starting 10 s before and ending 5 s after the main ScP pulse.

4.2. Inversions of Individual Events

As a first test, we inverted for ULVZ parameters of each event individually. Example individual inversions of events 5 and 6 (event numbers listed in the y-axis of Figure 10) for bin 37 are shown in Figure 12. In this bin, these two events have a large precursor-like arrival at ~5 s before the ScP arrival, which is within the expected range of ScP pre-cursors. However, this arrival is not apparent in the seismograms for the other events in this bin and

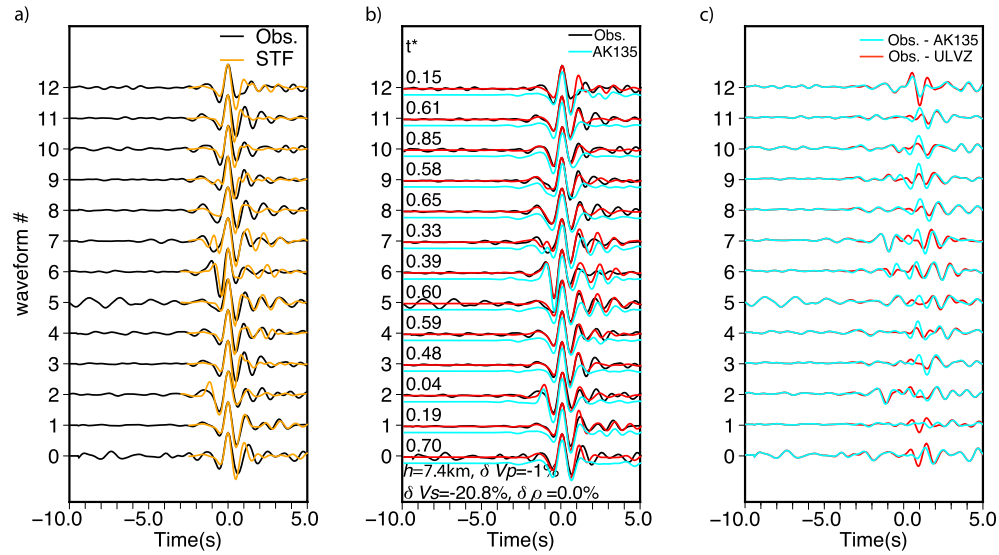

Figure 9. Data and inversion results for bin 24. (a) ScP waveforms (black lines) and P-wavelets (orange lines) used as source time function are shown. In this bin, recordings from 13 events were used (numbered along the left-hand side of the panel). Each waveform represents the stack of vertical component velocity seismograms which is obtained by aligning waveforms using adaptive stacking (Rawlinson & Kennett, 2004), and the stacked waveform is normalized to unity. (b) The ScP waveforms (black) are shown with overlays of the synthetic predictions for the best-fit Ultralow-velocity zone (ULVZ) model (red traces) and AK135 predictions (cyan traces). The AK135 predictions (cyan trace) in (b) are slightly offset for visualization purpose only. The t^* value obtained from the inversion is shown just above each trace and the best-fit ULVZ parameters are shown at the bottom of the panel. (c) Residuals for ULVZ predictions (red lines) and AK135 predictions (cyan lines). Note that waveform amplitude scaling is same for all the panels.

is likely noise. Nevertheless, the individual inversions attempt to fit these arrivals as ScP precursors. For event 5, this results in a strong P-wave velocity drop ($\delta V_P = -44.1\%$) which is more than twice as large as the recovered S-wave velocity perturbation ($\delta V_S = -19.4\%$) which is likely not correct. In the case of event 6 this results in a large ULVZ thickness ($h = 29.9$ km) and a strong density perturbation ($\delta\rho = +28.1\%$). Moreover, the ULVZ parameters differ significantly between these two events even though they are from the same bin and sample nearly the same location on the CMB.

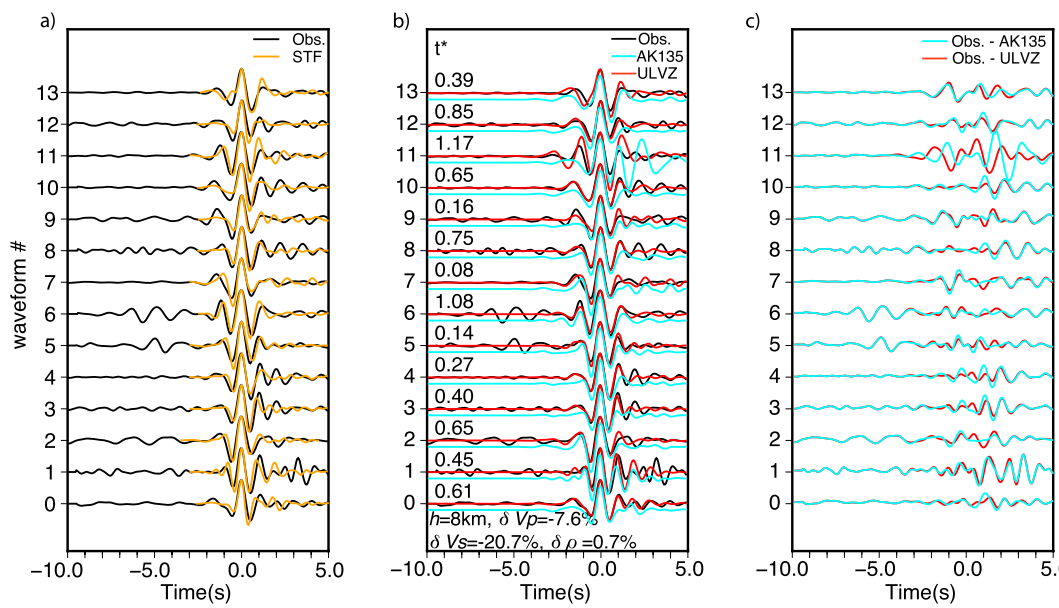

Figure 10. Same as Figure 9 but for bin 37.

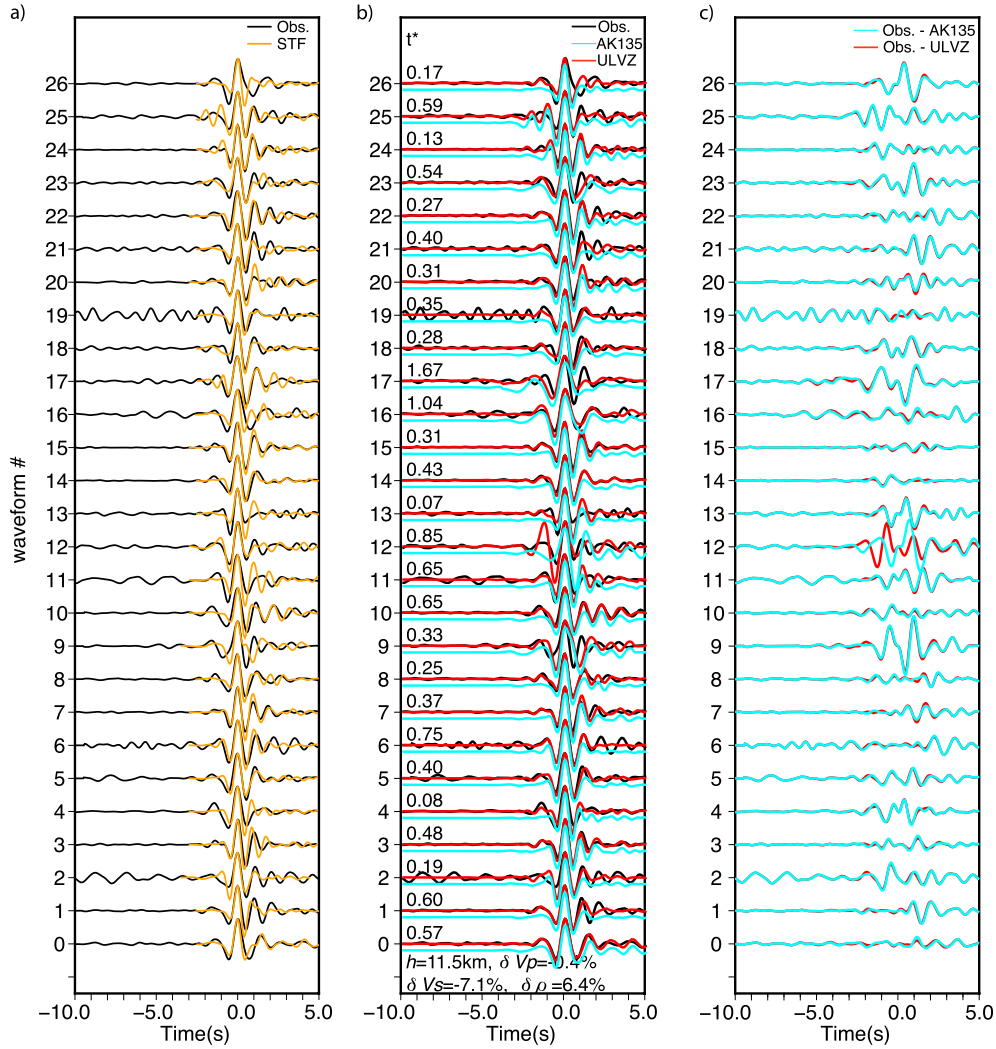

Figure 11. Same as Figure 9 but for bin 41.

As the previous example demonstrates, inversion of individual events can lead to widely disparate ULVZ models and the physical interpretation of these ULVZ structures becomes challenging. In this inversion test, we found that the P-wave velocity and density perturbations were often unreasonably high. In most cases, the P-wave velocity perturbation was stronger than the S-wave velocity perturbation (e.g., event 5 in bin 37). This is because the P-wave velocity and density are mostly constrained by the precursors, which can be over amplified, or even completely erroneous, due to the stacking of coherent noise in the data. Although the ULVZ elastic parameters

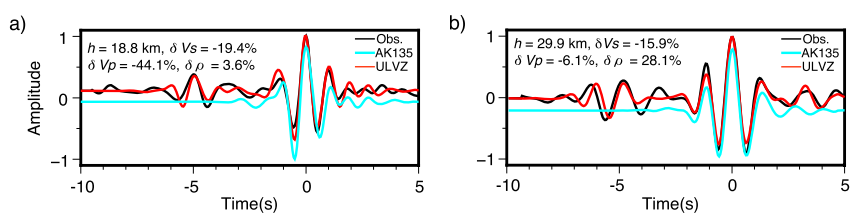

Figure 12. Example inversion results for bin 37 for (a) event 5 and (b) event 6 (see Figure 10). Shown in both panels are predictions for best-fit Ultralow-velocity zone (ULVZ) model (red trace) and AK135 (cyan trace) overlain on the observed ScP waveform (black trace). The AK135 prediction (cyan trace) is slightly offset for visualization purpose only. ULVZ parameters obtained from the inversions are presented in both panels. All traces are normalized and are vertical component velocity seismograms.

are biased by the presence of noise, we find that the attenuation (t^* parameter) appears well-constrained in the individual inversions. As discussed in the next section, including t^* as a free parameter in the inversion, significantly increases how much time is required for the inversion to converge. Therefore, in the third inversion test, we used the t^* parameter obtained from the individual inversions as an attempt to speed up convergence.

4.3. Joint Inversion of Multiple Events With t^* Fixed

In the previous section we showed that the ULVZ parameters recovered in our inversions varied significantly within a single geographic bin and often gave unreasonably high P-wave velocity and density perturbations. Therefore, in our next test we jointly inverted all events occurring within a bin. In this test, we fixed t^* with the values obtained from the individual event inversions described in Section 4.2, which gives rapid convergence of ULVZ parameters.

In the implementation of the joint inversion, attenuation and convolution with the appropriate STF are performed for each waveform separately. This step is necessary as we expect that the t^* operator and STF are unique for each event. After this step, these waveforms are compared with the observed ScP waveforms. Example joint inversion results for bins 24, 37, and 41 are shown in Figures 9b–9c, 10b–10c, and 11b–11c, respectively. ULVZ parameters estimated from the inversion (i.e., the maximum likelihood model) are shown on the bottom of each plot which shows that ∼20% decrease in S-wave velocity is required to explain the observed ScP waveforms for bins 24 and 37 (Figures 9b–9c and 10b–c) but only a ∼7% decrease for bin 41 (Figures 11b–11c). The results shown in bin 24 exemplify a bin where a ULVZ structure appears necessary. In this bin we can clearly see an ScsP post-cursor (peak arrival time occurs at ∼1.5 s) in the observations (black traces in Figure 9b) that does not occur in the AK135 predictions (blue traces). However, this post-cursor is predicted by the maximum likelihood ULVZ model (red traces). In contrast, the predicted waveforms for AK135 and ULVZ models are almost identical for most of the events in bin 41 (Figures 11b–11c). Importantly, the predicted waveforms do not give as high a preference to models that appear to contain high noise. For example, the potential noise-related precursor discussed in the previous section (events 5 and 6 in bin 37) are not fit in the joint inversion (Figure 10b). But the joint inversion gives preference to those features that are coherent in all the events. Thus, the joint inversion approach prevents overfitting of coherent noise in the data, thereby providing more robust estimates of the ULVZ parameters. Additionally, we see that the joint inversion provides significantly lower amplitude P-wave velocity perturbations than the individual inversions (mostly higher than S-wave velocity perturbations), suggesting that the individual inversions were indeed impacted by fitting of noise in the pre-cursory wavefield.

Inversion results expressed in terms of the maximum likelihood model and the uncertainties expressed in terms of standard deviation from the PPD for elastic parameters (δV_S, δV_P, $\delta\rho$, and h) are presented in Table S1 in Supporting Information S1. In addition, the maximum likelihood values are also plotted in Figures 13a–13e. The inversion can identify thin and weak ULVZs that do not produce visible pre- and post-cursors. Therefore, the ULVZs identified here can be as thin as 1 km with a strong decrease in δV_S, which modulates the pulse width of the ScP phase and improves the fit between observed and predicted data. Similarly, the inversion can identify thicker ULVZs with weaker δV_S. For example, from the visual inspection of P and ScP wavelets, it is difficult to tell whether bin 41 requires ULVZ structure, and our inversion results for this bin suggest a 11.5-km thick ULVZ with a 7.1% decrease in S-wave velocity. The inversion results for bin 7 suggest a 22.5-km thick ULVZ with a 3.9% reduction in δV_S. In contrast, the inversion results for bin 49 show a 1.5-km thick ULVZ with a 50% reduction in δV_S. Thus, a significant challenge in interpreting these results is how to define what is a ULVZ. Therefore, as another measure we also define the ULVZ strength as ULVZ thickness multiplied by δV_S in order to represent the combined effect of ULVZ thickness and δV_S, and present in Figure 13f. This is similar to the ULVZ strength parameter defined in Pachhai, Thorne, et al. (2022) and Rondenay et al. (2010) and provides another way of assessing whether or not a ULVZ is required to fit these data. Qualitatively, we observe that when looking at the data in individual geographic bins that we can identify an ScsP post-cursor that does not exist in the AK135 predictions when the ULVZ strength is at or above approximately 150 km%. Recall, that for the case of bin 24, we could clearly identify an ScsP post-cursor in the observations, and we see that the maximum likelihood model for bin 24 gives a ULVZ strength of 154 km%. On the other-hand, bin 41 which appears by eye to be well-fit by the AK135 prediction has a maximum likelihood ULVZ model with a ULVZ strength of 81 km%. Thus, we center the color palette table in Figure 13f at a strength of 150 km%. This is admittedly a somewhat qualitative boundary between ULVZ (red shading) and non-ULVZ (blue shading) but is based on visual inspection of the waveforms.

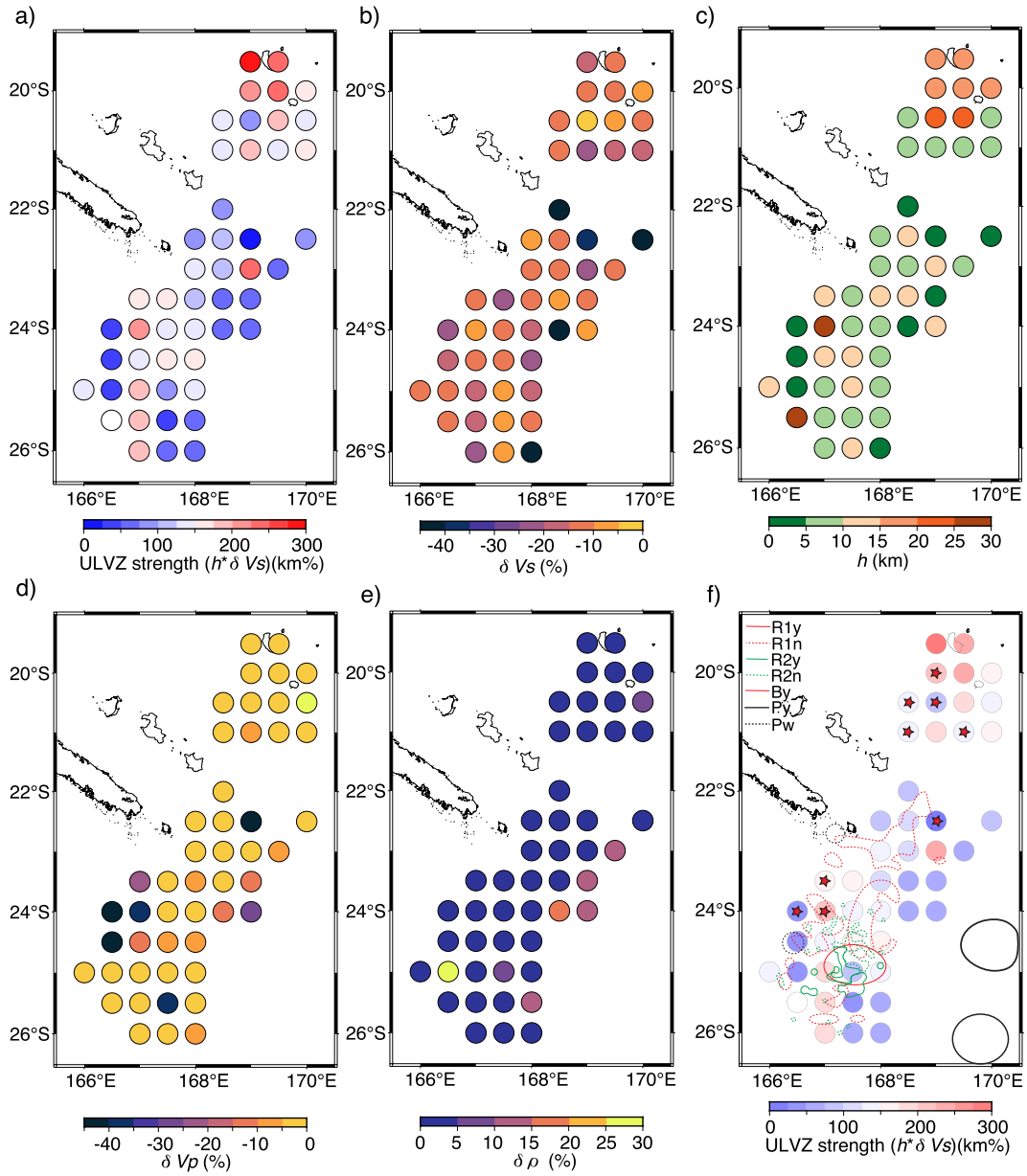

Figure 13. Inversion results for the test where we fixed the t^* parameters from the individual inversions. In each plot the estimated Ultralow-velocity zone (ULVZ) parameters are drawn as shaded circles at the geographic center. (a) ULVZ strength expressed in terms of the product of δV_S and h, (b) δV_S, (c) h, (d) δV_P, (e) $\delta\rho$, and (f) results from previous ScP studies overlain on top of the ULVZ strength (opacity is decreased to highlight the results from the past studies) plot. R1y—ScP precursor observed in Rost et al. (2005), R1n—ScP precursor not observed in Rost et al. (2005), R2y—ULVZ observed in Rost, Garnero, et al. (2006), R2n—ULVZ not observed in Rost, Garnero, et al. (2006), By—ULVZ observed in Brown et al. (2015), Py—ULVZ observed in Pachhai, Li, et al. (2022), and Pw—weak ULVZ observed in Pachhai, Li, et al. (2022). Star symbol indicates the bin locations where extra post-cursor appears that cannot be explained by 1-D prediction.

As we can see in Figure 13, there is evidence for the existence of ULVZs across the entire study site from North to South. Recovered ULVZ thickness varies from less than a kilometer to 29.9 km while the δV_S varies between roughly -50%–-4%. The large velocity decreases of -50% occur in bins with extremely small thicknesses that are on the order of 1.5 km. These bins have some of the lowest ULVZ strengths and may not actually require ULVZ structure to explain these data (e.g., bin 49 has $\delta V_S = -50\%$, $h = 1.5$ km, and strength = 74 km%), which makes interpretation of these results purely in terms of inverted elastic parameters challenging. We observe a weak variation of δV_P and $\delta\rho$, and values are mostly lower than 10% except in the case of bins 17, 23, 33, 34, and

45 for P-wave velocity and bin 39 for density. In contrast to the inversions for individual events, we found that δV_P is lower in magnitude than that for δV_S, and $\delta\rho$ are also below 10% in most bins. These data separate into northern bins (bins 1–13) and southern region (bins 14–49) and the ULVZ properties appear slightly different between them but are roughly consistent within a region.

In the northern region the evidence for ULVZ structure is most apparent for those bins along the eastern side (bins 1–5, 8, 11–13). In these ULVZ-like bins we see a variation in δV_S reduction from the maximum likelihood models from ∼9%–21% with an average of $\delta V_S = -13.4\%$. The thickness varies from roughly 9–20 km with an average of $h = 16.7$ km. The maximum likelihood model for these bins shows negligible P-wave velocity and density perturbations. The bins on the western boundary (bins 3, 6, 7, and 10) are striking in that they appear to show added complexity in the post-cursor wavefield. In particular, they show an additional post-cursor that is not reproduced by 1-D ULVZ models.

In the southern region we estimate ULVZ properties in bins with ULVZ strength ≥130 km% (bins 19, 21, 23, 24, 29, 31, 35–38, 40, 42–44, 47). In these ULVZ-like bins we see a variation in δV_S reduction from the maximum likelihood models from ∼6%–37% with an average of $\delta V_S = -15\%$ if we discard some of the ULVZ with $\delta V_S = -50.0\%$. The thickness varies from roughly 1–30 km with an average of $h = 9.5$ km. P-wave velocity reductions are mostly small in the southern region also and are mostly less than 10%. However, a few bins show relatively large δV_P and $\delta\rho$. Additional bins on the western boundary of the study region (bins 23, 28, and 29) also show additional post-cursor arrivals.

In the northern region δVS is about −13% and ∼15 km thick, whereas in the southern region the S-wave velocity and thickness are more variable but tend to slightly larger S-wave velocity reductions (which often exceed −20%), but average out to approximately −15% and slightly thinner at ∼9.5 km. In both regions δV_P is mostly between −5% and −10%. Overall, these results support a slightly thicker ULVZ in the north with slightly reduced S-wave velocity perturbation when compared to ULVZ structures observed in the south.

Figure 13f shows locations where ULVZs have been inferred from previously published results overlain on the ULVZ strength map. We broadly observe ULVZ structure in the southern part of our study region where past studies have also indicated ULVZs. However, our results suggest that the region is more broadly ULVZ-like and less patchy than previous studies would indicate. Furthermore, we show ULVZ evidence in the northern portion of our study region where no ULVZs have been previously identified. We provide a more detailed comparison between these and previous results in Section 5 of this paper.

4.4. Full Joint Inversion

In our third test, we also applied the Bayesian inversion approach to all the bins with waveforms for more than five events by sampling both t^* and ULVZ parameters. However, for several bins the inversion did not converge, even after collecting more than 200,000 models in several weeks. We check convergence by monitoring the likelihood values for all the sampling history. In the case of converged solution, the likelihood remains stable after reaching the maximum likelihood, but the likelihood keeps increasing even after 100,000 s of iterations for the inversions that are not converged. One of the reasons these inversions do not converge is that these bins have many more parameters to be sampled as those bins that have large numbers of events. This is because the number of parameters to be explored increased by three for each additional event (standard deviation of noise, AR1 coefficient, and t^* parameter) in a bin. Additionally, the t^* value and noise parameters are different for individual events although they sample within ∼50-km distance at the CMB. This is because the t^* value not only includes the path attenuation effect, but it also includes the source- and receiver-side effects. This means that t^* values represent the effective attenuation rather than just an attenuation along the path. Similarly, the noise level is also different for different events. Table S2 in Supporting Information S1 summarizes the results from this test. Inversion results that did not converge are indicated. Comparison of values from Tables S1 and S2 in Supporting Information S1 indicates that inversion results do not change significantly in most bins. Results differ significantly from these two inversions are marked by bold fonts in Table S2 in Supporting Information S1.

5. Discussion

For most events examined in this study, we observe that the ScP pulse width is larger than that for the direct P-wave (e.g., see Figure 1). This is because the ScP pulse width can be broadened due to the attenuation of ScP

waves in the lower mantle, or due to the interaction of ScP with ULVZ structures. However, only a handful of previous studies have considered the attenuation of the ScP pulse as a part of their ULVZ modeling (Hansen et al., 2020; Rost et al., 2005; Thorne et al., 2021). These studies first determined a t^* operator that best-fit the ScP pulse width assuming that the broadening of the ScP pulse is only due to attenuation. But this assumption may not be valid as ULVZ structure can also broaden the ScP pulse width. This problem may be especially evident for thin ULVZs, in which the primary method of detection would be through detection of a broadened ScP pulse. If a thin ULVZ exists, it will likely go undetected when attenuation is first modeled as separate from ULVZ structure.

This study addresses this challenge by developing a Bayesian inversion of ScP data that also considers the path attenuation as an unknown parameter. To address the cause of different pulse widths of P and ScP waveforms, we incorporate the t^* parameter in the forward modeling through a hierarchical Bayesian model. This means that the P wavelet is first attenuated using the t^* value sampled by the algorithm and convolved with the Green's function computed for ULVZ parameters. This approach does not force attenuation or ULVZ structure onto the model to match the pulse width. In contrast, the data determine the appropriate Earth model structure as well as the appropriate attenuation. As there exists an intrinsic trade-off between the attenuation and Earth structure that can be resolved by ScP data, we performed inversions including t^* parameters as well as inversions without considering t^* in the inversion. Inversion of synthetic predictions shows retrieval of incorrect ULVZ parameters when we ignore t^* parameters, particularly when the t^* value is high (Figure 5). This is because additional structure is required to create the ScP pulse widening when the t^* parameter is not considered.

A significant challenge in modeling ScP waveforms is that the amplitude and arrival times of the pre- and post-cursors vary even within a 0.5° radius on the CMB (e.g., Figures 9–11). Previous studies have also indicated such small-scale variability with the appearance or non-appearance of ScP precursors occurring within a few 10s of kilometers on the CMB of each other (Rost et al., 2005; Rost, Garnero, et al., 2006). Our inversion results for individual events also demonstrated a high degree of variability. This is because our inversion tries to fit large amplitude pre- and post-cursor like features after fitting the main ScP arrival, whether or not those features are true pre- or post-cursors. Noise in the data is a significant challenge as it can become coherent due to filtering and stacking of waveforms from individual stations. This affects the results of δV_P more so than that of δV_S as the P-wave velocity is determined through relatively low amplitude pre-cursor arrivals. Although we address correlated data noise using the first-order autoregressive (AR1) model, higher-order correlated noise may not be captured in our modeling. Therefore, the inversion may not be able to prevent fitting correlated noise which interferes with our ability to recover P-wave velocities. In some cases, the effect appeared especially egregious, and our inversion would infer δV_P with greater magnitude than δV_S. This effect was observed even after considering the t^* parameter in the inversion. To address this challenge, previous studies stacked ScP wavelets from multiple events to estimate the ULVZ parameters (Rost et al., 2005). But this requires high quality events with similar sources for all the events considered (i.e., P wavelets). As a result, only a limited number of events can be considered for the analysis.

Here we applied joint inversion of ScP data from multiple events to overcome this challenge. In this case, the individual waveforms are not fit as well as they are when each event is individually inverted. But the inversion results are more stable and do not appear to over-fit the data, rather the inversion focuses on the arrivals that are coherent in all events. Nonetheless, the inversion takes considerably more time to converge. As the attenuation of the ScP wavelet is dependent on the respective P wavelet, the number of unknowns increases with the number of waveforms within a bin. We also note that we have two more parameters for each ScP waveform (one for the standard deviation of noise and the other for the AR1 parameter that represents the width of correlation). Because the inversion struggles to find the balance between fit and the number of unknowns considered in the inversion, we had difficulty obtaining convergence when there were close to 30 waveforms within a bin.

The southwestern area of our study region has been previously studied using a variety of ScP data sets. The locations of these previous studies are shown in Figure 13f. There are many common locations where the detection of ULVZs is unclear, mainly in the center around -25^{o} latitude. Here we see variability in the sense that not all studies agree as to whether a ULVZ is required in this location or not, and we also see evidence against ULVZ presences with a few km on the CMB. This is likely because those studies analyzed ScP waveforms using one event at a time. Our inversion results show equally scattered ULVZ parameter values when we run inversions for individual events. The inversion results obtained for ScP waveforms from individual event suggest many extreme values for δV_S ($\sim -50\%$). This is because the inversion tries to fit the large features in the waveforms first which

is the central pulse of ScP. If the attenuated P wave does not fit the overall ScP waveform including the central pulse, inversion increases δVs within a thin layer to achieve a better fit. The inversion can also increase δVp to overfit the dominant coherent noise in the precursor wavefield (e.g., Figure 12).

One of the challenges in this work, and in ULVZ waveform studies in general, is in determining whether or not ULVZ structure is significantly warranted. An over-parameterized model, with complex ULVZ structure, can improve the data fit but may not necessarily be required. Similarly, an under-parameterized model may only explain part of the data. This means that both under- and over-parameterized models can give biased estimates of ULVZ structures. Therefore, appropriate model selection is crucial to make a judgment on whether we need a ULVZ model to explain the data. We tested various statistical criteria including the Bayesian Information Criterion (e.g., Pachhai et al., 2014; BIC = $-2 * \log(L) + M * \log(npts)$, where L is the likelihood, and M is the number of model parameters), variance reduction (i.e., $1 - \frac{\sum_{i=1}^{npts} (d^{obs} - d^{pred})^2}{\sum_{i=1}^{npts} (d^{obs})^2}$, where $npts$ is the number of data points), and variance ratio. However, none of these criteria provided conclusive results in selecting whether the ULVZ models were necessary. One of the reasons, that the BIC may fail to identify the correct model, is that the BIC considers a single value of likelihood that maximizes the posterior, but in the inversion, there are several other models within a prior range that explain the observed data. Additionally, the noise model we considered in the likelihood function in Equation 4 is an autoregressive (AR1) model, which is equivalent to an exponentially decaying covariance matrix. However, in practice such a noise model may fail to fully represent the unknown noise in the data. If the noise model is simpler than the true noise model, more structure may be needed to explain the observed data and vice versa. Therefore, a more realistic noise model may be required in order to quantitively determine if the AK135 model is sufficient or if more complex ULVZ models are justified. Additionally, a more formal Bayesian model selection criterion using Bayesian evidence (denominator term of Equation 1) can be applied. This approach has been rarely attempted in seismic applications (e.g., Dettmer et al., 2010). However, the computation of Bayesian evidence is computationally intensive, particularly when we have a large number of events within a bin, as it needs to integrate over all the parameters. Our future work will address the computation of the evidence for Bayesian model selection.

In several of our geographic bins we observe additional post-cursor arrivals that are not predicted by our 1-D ULVZ models. The locations of the geographic bins that show clearly identifiable additional arrivals are marked by stars in Figure 13f. These additional arrivals are found in a time window where there should not be any contamination from other arrivals, and they are also not explained by complexity in the P-wavelet. As an example, Figure 14 shows the P and ScP waveforms for a single event where an additional coherent post-cursor is evident. In Figure 14a we show the direct P-wave, which may have some small coherent energy arriving at about 18 s behind the main P-wave arrival. But we see an additional ScP post-cursor at about 7 s after ScP (Figure 14b) which occurs much too early to be due to any observed complexity in the P-wavelet. We note that this event was not included in the inversion as there were less than five events in the bin that corresponds to this event. Although, additional post-cursory energy like this (for this example) arrives later in time than the time window we used in our inversion process, its existence could hint at higher dimensional ULVZ structure that we are not modeling in this study and provide an exciting opportunity to investigate ULVZ shape in future studies. It is highly unlikely that such a large amplitude postcursor is due to anisotropy in the Earth interior. Past studies show that the strongest anisotropy has been observed in the upper mantle with delay times between fast and slow propagation typically being less than ~1 s for SKS (e.g., Long & Silver, 2009). If the observed postcursors are due to anisotropy in the transition zone, significantly anisotropy of up to ~10% must exist in the transition zone in order to explain more than 5 s of time delay, similar to that shown in Figure 14. This is highly unlikely with only ~3% anisotropy observed in the transition zone (e.g., Trampert & van Heijst, 2002). Additionally, postcursors are observed not only for shallow events but also for deeper earthquakes. It is unlikely that the azimuthal anisotropy in the lowermost mantle (e.g., Garnero et al., 2004; Wookey et al., 2005) produces such strong postcursors. It is also unlikely that fine scale azimuthal anisotropy can produce coherent ScP postcursors as shown in Figure 14. We also inspected the S waveforms from both vertical and transverse components (Figures S8–S10 in Supporting Information S1) which suggests that our observations are not affected by anisotropic structure in the mantle or STF complexity.

ULVZ waveforms for a handful of 2-D models were first published in Brown et al. (2015) and showed additional post-cursor arrivals reminiscent of those we observe here. To understand the reason for an additional

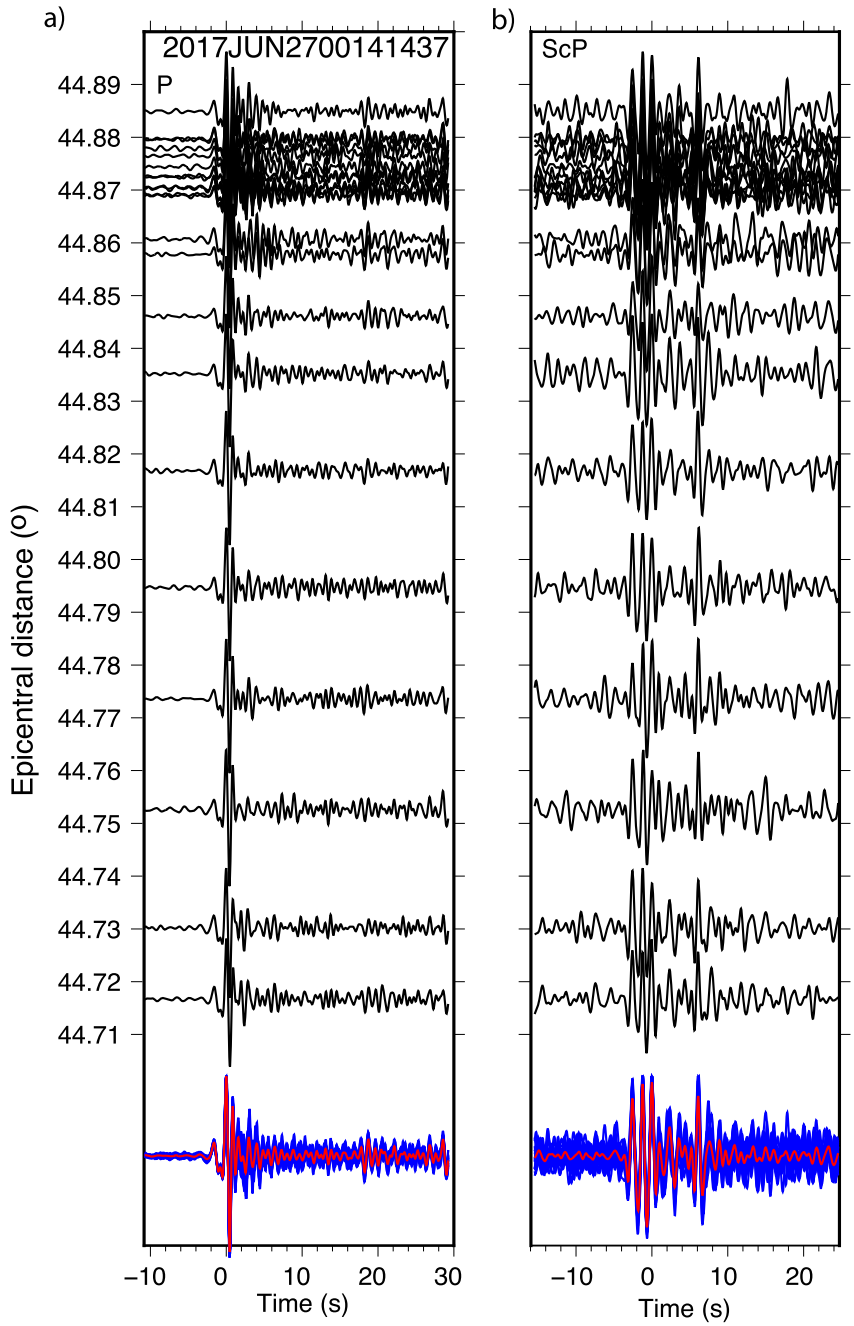

Figure 14. Example waveforms for (a) P and (b) ScP for a 132 km deep event occurring on 27 June 2017 recorded at Warramunga Array that show additional arrival near 7 s after the ScP. Each waveform (black) represents the vertical component velocity seismograms aligned using adaptive stacking (Rawlinson & Kennett, 2004). All waveforms are overlain in blue at the bottom of each panel and the stacked waveforms are shown in red.

ScP post-cursor, we computed synthetic ScP waveforms for a boxcar ULVZ using the 2.5-D PSVaxi code (e.g., Thorne et al., 2013). The schematic diagram and resulting waveforms for various ULVZ positions are shown in Figure 15. In addition to the ScsP postcursor predicted for 1-D models, there is an additional post-cursor that has a varying moveout with respect to ULVZ position. We reserve identification of these additional arrivals for a follow-up paper as the description is rather lengthy. However, the timing of these arrivals is closely linked to the boundaries of the ULVZs. What is important here is that in some cases, where the ScP bounce point is located away from the center of the ULVZ for this particular example, we can clearly observe an addi-

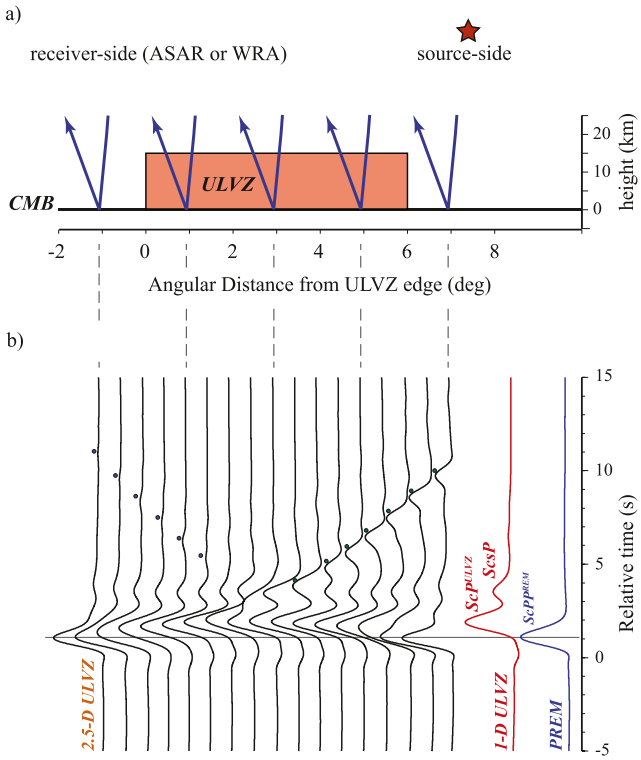

Figure 15. Example ScP waveforms for 2-D Ultralow-velocity zones (ULVZs). (a) Boxcar ULVZ of 6° length and 15 km height with 20% decrease in S-wave velocity, 10% decrease in P-wave velocity, and 5% increase in density. ULVZ height is exaggerated for visualization purpose. ScP ray paths (blue) interact with the ULVZ based on the location of the ULVZ-edge position. For example, if the angular distance to the ULVZ edge is 5° then the ScP ray bounces nearly in the center of the ULVZ as shown by the ScP ray path with bounce point at 5°. (b) Synthetic vertical component ScP displacement seismograms for PREM (blue line, Dziewonski & Anderson, 1981), 1-D ULVZ (red line), and 2.5-D ULVZs (black lines). 2.5-D ULVZ models are drawn in location relative to their edge positions and are aligned with the positions in panel (a). Synthetics are computed at 40° epicentral distance. Additional post-cursor arrivals that do not exist in the 1-D ULVZ model are marked by dots. Waveforms are aligned based on the PREM prediction.

tional post-cursor. But depending on ULVZ edge position this post-cursor may interfere with the ScsP postcursor modulating both its apparent arrival time and amplitude. Thus, if 2-D structure exists in our study region, it is possible that such arrivals are affecting our inversion results. We also note that in these 2.5-D synthetics that we observe the ScsP post-cursor and the additional post-cursors even in cases where the ScP ray does not directly strike the ULVZ. For example, if the ULVZ edge position is at 7° (Figure 15b) we observe a complicated waveform that exists of Equation 1 an ScP arrival coincident with the PREM prediction (ScP^{PREM}), (b) another lower amplitude ScP arrival coincident in time with the prediction for ScP traveling through the ULVZ (ScP^{ULVZ}), (c) the normal ScsP post-cursor, and (d) the additional edge-related post-cursor. The two ScP arrivals occur due to multi-pathing near the ULVZ edge. Thus, the ScP waveforms could be extremely complicated in the presence of 2-D structure. While it is possible that additional post-cursors we observe in our data can be related to 2-D/3-D ULVZ shape, we also note that these observations can also be due to the layering of ULVZ structures (e.g., Idehara, 2011; Pachhai, Li, et al., 2022; Ross et al., 2004; Thybo et al., 2003).

6. Conclusions

We developed a joint Bayesian inversion of ScP waveforms for multiple events. To address the ScP path attenuation, we considered the attenuation parameters (t^*) as unknown parameters in the inversion. We first applied this approach to a series of tests using synthetic predictions for weak, moderate, and strong ULVZs with various levels of complexity in the STF. Our inversion for these synthetic tests shows that the inversion can retrieve incorrect ULVZ parameters if we do not include the attenuation parameters in the inversion, particularly when the attenuation is strong in ScP waveforms. Additionally, we found that the ULVZ parameters determined in the inversion of a single event can be incorrect when the STF is complex and/or if there is coherent noise in the ScP precursory wavefield. In both scenarios the inversion scheme can overfit these spurious arrivals. To reduce the effect of coherent noise in the inversion, we applied joint inversion of ScP waveforms from multiple events. Inversion of multiple events reduces the impact of coherent noise or STF complexity in one or more traces. We applied these new inversion techniques to a newly collected suite of recordings for data with ScP bounce points beneath the Coral Sea. Here we find evidence for ULVZ existence across the entire region, but we find variation in ULVZ parameters throughout. This variation could be due to rapid spatial variation in ULVZ elastic parameters or possibly due to the effects on ScP waves resulting from the 2-D/3-D shape of ULVZs. These higher-dimensional shape effects are not captured in this inversion as a computationally efficient forward approach to predict the ScP waveforms in 2- or 3-D does not yet exist. Moreover, additional ScP post-cursor arrivals are predicted in 2-D ULVZ models that do not exist in the 1-D forward models. Additional, post-cursor arrivals are observed in these data beneath the Coral Sea which could indicate that we may be observing either 2D/3D ULVZ structural effects or internal layering of ULVZs (e.g., Pachhai, Li, et al., 2022). Investigation of these two scenarios requires more significant computational efforts and is the subject of future work.

Data Availability Statement

All the waveform data used in this study are publicly available through uhive (https://hive.utah.edu), University of Utah Research Data Repository: https://doi.org/10.7278/S50d-a67s-y717. Record sections for observed and predicted ScP waveforms from each bin are also available through the same link.

Acknowledgments
We would like to thank the editor, Michael Bostock, the associate editor, Satoru Tanaka, and an anonymous reviewer for providing constructive comments that improved our manuscript. We acknowledge the University of Utah Center for High Performance Computing (CHPC) for computing resources and support. MT and SP were partially funded by NSF Grants EAR 1723081 and 2139966. SR was partially supported by NSFGEO-NERC Grant NE/R012199/1. The facilities of IRIS Data Services, and specifically the IRIS Data Management Center, were used to access waveforms, related metadata, and/or derived products used in this study. IRIS Data Services are funded through the Seismological Facilities for the Advancement of Geoscience and EarthScope (SAGE) Proposal for the National Science Foundation under Cooperative Agreement EAR-1261681.

References

Aki, K., & Richards, P. G., (2002). Quantitative seismology.
Andrault, D., Pesce, G., Bouhifd, M. A., Bolfan-Casanova, N., Hénot, J.-M., & Mezouar, M. (2014). Melting of subducted basalt at the core-mantle boundary. *Science*, *344*(6186), 892–895. https://doi.org/10.1126/science.1250466
Avants, M., Lay, T., & Garnero, E. J. (2006). A new probe of ULVZ S-wave velocity structure: Array stacking of ScS waveforms. *Geophysical Research Letters*, *33*(7), L07314. https://doi.org/10.1029/2005gl024989
Berryman, J. G. (2000). Seismic velocity decrement ratios for regions of partial melt in the lower mantle. *Geophysical Research Letters*, *27*(3), 421–424. https://doi.org/10.1029/1999gl008402
Bréger, L., & Romanowicz, B. (1998). Three-dimensional structure at the base of the mantle beneath the central Pacific. *Science*, *282*(5389), 718–720. https://doi.org/10.1126/science.282.5389.718
Brown, S. P., Thorne, M. S., Miyagi, L., & Rost, S. (2015). A compositional origin to ultralow-velocity zones. *Geophysical Research Letters*, *42*(4), 1039–1045. https://doi.org/10.1002/2014gl062097
Buffett, B. A., Garnero, E. J., & Jeanloz, R. (2000). Sediments at the top of Earth's core. *Science*, *290*(5495), 1338–1342. https://doi.org/10.1126/science.290.5495.1338
Chapman, C., & Orcutt, J. (1985). The computation of body wave synthetic seismograms in laterally homogeneous media. *Reviews of Geophysics*, *23*(2), 105–163. https://doi.org/10.1029/rg023i002p00105
Choy, G. L. (1977). Theoretical seismograms of core phases calculated by frequency-dependent full wave theory, and their interpretation. *Geophysical Journal International*, *51*(2), 275–312. https://doi.org/10.1111/j.1365-246x.1977.tb06921.x
Cottaar, S., Martin, C., Li, Z., & Parai, R. (2022). The root to the Galápagos mantle plume on the core-mantle boundary.
Cottaar, S., & Romanowicz, B. (2012). An unsually large ULVZ at the base of the mantle near Hawaii. *Earth and Planetary Science Letters*, *355*, 213–222. https://doi.org/10.1016/j.epsl.2012.09.005
Dettmer, J., & Dosso, S. E. (2012). Trans-dimensional matched-field geoacoustic inversion with hierarchical error models and interacting Markov chains. *The Journal of the Acoustical Society of America*, *132*(4), 2239–2250. https://doi.org/10.1121/1.4746016
Dettmer, J., Dosso, S. E., & Osler, J. C. (2010). Bayesian evidence computation for model selection in non-linear geoacoustic inference problems. *The Journal of the Acoustical Society of America*, *128*(6), 3406–3415. https://doi.org/10.1121/1.3506345
Dettmer, J., Molnar, S., Steininger, G., Dosso, S. E., & Cassidy, J. F. (2012). Trans-dimensional inversion of microtremor array dispersion data with hierarchical autoregressive error models. *Geophysical Journal International*, *188*(2), 719–734. https://doi.org/10.1111/j.1365-246x.2011.05302.x
Dobson, D. P., & Brodholt, J. P. (2005). Subducted banded iron formations as a source of ultralow-velocity zones at the core–mantle boundary. *Nature*, *434*(7031), 371–374. https://doi.org/10.1038/nature03430
Dziewonski, A. M. (1984). Mapping the lower mantle: Determination of lateral heterogeneity in P velocity up to degree and order 6. *Journal of Geophysical Research*, *89*(B7), 5929–5952. https://doi.org/10.1029/jb089ib07p05929
Dziewonski, A. M., & Anderson, D. L. (1981). Preliminary reference Earth model. *Physics of the Earth and Planetary Interiors*, *25*(4), 297–356. https://doi.org/10.1016/0031-9201(81)90046-7
Futterman, W. (1962). Dispersive body waves. *Journal of Geophysical Research*, *67*(13), 5279–5291. https://doi.org/10.1029/jz067i013p05279
Garnero, E. J. (2000). Heterogeneity of the lowermost mantle. *Annual Review of Earth and Planetary Sciences*, *28*(1), 509–537. https://doi.org/10.1146/annurev.earth.28.1.509
Garnero, E. J., Grand, S. P., & Helmberger, D. V. (1993). Low P-wave velocity at the base of the mantle. *Geophysical Research Letters*, *20*(17), 1843–1846. https://doi.org/10.1029/93gl02009
Garnero, E. J., & Helmberger, D. V. (1995). A very slow basal layer underlying large-scale low-velocity anomalies in the lower mantle beneath the Pacific: Evidence from core phases. *Physics of the Earth and Planetary Interiors*, *91*(1–3), 161–176. https://doi.org/10.1016/0031-9201(95)03039-y
Garnero, E. J., & Helmberger, D. V. (1998). Further structural constraints and uncertainties of a thin laterally varying ultralow-velocity layer at the base of the mantle. *Journal of Geophysical Research*, *103*(B6), 12495–12509. https://doi.org/10.1029/98jb00700
Garnero, E. J., Maupin, V., Lay, T., & Fouch, M. J. (2004). Variable azimuthal anisotropy in Earth's lowermost mantle. *Science*, *306*(5694), 259–261. https://doi.org/10.1126/science.1103411
Garnero, E. J., McNamara, A. K., & Shim, S.-H. (2016). Continent-sized anomalous zones with low seismic velocity at the base of Earth's mantle. *Nature Geoscience*, *9*(7), 481–489. https://doi.org/10.1038/ngeo2733
Garnero, E. J., Revenaugh, J., Williams, Q., Lay, T., & Kellogg, L. H. (1998). Ultralow velocity zone at the core-mantle boundary. In *The core-mantle boundary region* (Vol. 28, pp. 319–334).
Gilks, W. R., & Roberts, G. O. (1996). Strategies for improving MCMC. In *Markov chain Monte Carlo in practice* (Vol. 6, pp. 89–114).
Glanville, H., & Geoscience Australia. (2011). Australian National Seismograph Network Data Collection (Version 2.0, September 2018) [Dataset]. Geoscience Australia. Retrieved from https://ecat.ga.gov.au/geonetwork/srv/eng/catalog.search#/metadata/144675
Grand, S. P. (2002). Mantle shear–wave tomography and the fate of subducted slabs. *Philosophical Transactions of the Royal Society of London, Series A: Mathematical, Physical and Engineering Sciences*, *360*(1800), 2475–2491. https://doi.org/10.1098/rsta.2002.1077
Grand, S. P., Van der Hilst, R. D., & Widiyantoro, S. (1997). High resolution global tomography: A snapshot of convection in the Earth. *Geological Society of America Today*, *7*.
Hansen, S. E., Carson, S. E., Garnero, E. J., Rost, S., & Yu, S. (2020). Investigating ultra-low velocity zones in the southern hemisphere using an Antarctic dataset. *Earth and Planetary Science Letters*, *536*, 116142. https://doi.org/10.1016/j.epsl.2020.116142
Havens, E., & Revenaugh, J. (2001). A broadband seismic study of the lowermost mantle beneath Mexico: Constraints on ultralow velocity zone elasticity and density. *Journal of Geophysical Research*, *106*(B12), 30809–30820. https://doi.org/10.1029/2000jb000072
He, Y., & Wen, L. (2009). Structural features and shear-velocity structure of the "Pacific Anomaly". *Journal of Geophysical Research*, *114*(B2), B02309. https://doi.org/10.1029/2008jb005814
Hedlin, M. A., Shearer, P. M., & Earle, P. S. (1997). Seismic evidence for small-scale heterogeneity throughout the Earth's mantle. *Nature*, *387*(6629), 145–150. https://doi.org/10.1038/387145a0
Hosseini, K., Sigloch, K., Tsekhmistrenko, M., Zaheri, A., Nissen-Meyer, T., & Igel, H. (2020). Global mantle structure from multifrequency tomography using P, PP and P-diffracted waves. *Geophysical Journal International*, *220*(1), 96–141. https://doi.org/10.1093/gji/ggz394
Hu, Q., Kim, D. Y., Yang, W., Yang, L., Meng, Y., Zhang, L., & Mao, H.-K. (2016). FeO 2 and FeOOH under deep lower-mantle conditions and Earth's oxygen–hydrogen cycles. *Nature*, *534*(7606), 241–244. https://doi.org/10.1038/nature18018

Idehara, K. (2011). Structural heterogeneity of an ultra-low-velocity zone beneath the Philippine Islands: Implications for core–mantle chemical interactions induced by massive partial melting at the bottom of the mantle. *Physics of the Earth and Planetary Interiors*, *184*(1–2), 80–90. https://doi.org/10.1016/j.pepi.2010.10.014

Idehara, K., Yamada, A., & Zhao, D. (2007). Seismological constraints on the ultralow velocity zones in the lowermost mantle from core-reflected waves. *Physics of the Earth and Planetary Interiors*, *165*(1–2), 25–46. https://doi.org/10.1016/j.pepi.2007.07.005

Jenkins, J., Mousavi, S., Li, Z., & Cottar, S. (2021). A high-resolution map of Hawaiian ULVZ morphology from ScS phases. *Earth and Planetary Science Letters*, *563*, 116885. https://doi.org/10.1016/j.epsl.2021.116885

Kennett, B. L., Engdahl, E., & Buland, R. (1995). Constraints on seismic velocities in the Earth from traveltimes. *Geophysical Journal International*, *122*(1), 108–124. https://doi.org/10.1111/j.1365-246x.1995.tb03540.x

Kim, D., Lekić, V., Ménard, B., Baron, D., & Taghizadeh-Popp, M. (2020). Sequencing seismograms: A panoptic view of scattering in the core-mantle boundary region. *Science*, *368*(6496), 1223–1228. https://doi.org/10.1126/science.aba8972

Krier, J., Thorne, M. S., Leng, K., & Nissen-Meyer, T. (2021). A compositional component to the Samoa ultralow-velocity zone revealed through 2- and 3-D waveform modeling of SKS and SKKS differential travel-times and amplitudes. *Journal of Geophysical Research: Solid Earth*, *126*(7), e2021JB021897. https://doi.org/10.1029/2021JB021897

Labrosse, S., Hernlund, J., & Coltice, N. (2007). A crystallizing dense magma ocean at the base of the Earth's mantle. *Nature*, *450*(7171), 866–869. https://doi.org/10.1038/nature06355

Lay, T., & Garnero, E. J. (2011). Deep mantle seismic modeling and imaging. *Annual Review of Earth and Planetary Sciences*, *39*(39), 91–123. https://doi.org/10.1146/annurev-earth-040610-133354

Li, J., Sun, D., & Bower, D. J. (2022). Slab control on the mega-sized North Pacific ultra-low velocity zone. *Nature Communications*, *13*, 1–11. https://doi.org/10.1038/s41467-022-28708-8

Liu, J., Li, J., Hrubiak, R., & Smith, J. S. (2016). Origins of ultralow velocity zones through slab-derived metallic melt. *Proceedings of the National Academy of Sciences*, *113*(20), 5547–5551. https://doi.org/10.1073/pnas.1519540113

Long, M. D., & Silver, P. G. (2009). Shear wave splitting and mantle anisotropy: Measurements, interpretations, and new directions. *Surveys in Geophysics*, *30*(4–5), 407–461. https://doi.org/10.1007/s10712-009-9075-1

Mao, W. L., Mao, H.-K., Sturhahn, W., Zhao, J., Prakapenka, V. B., Meng, Y., et al. (2006). Iron-rich post-perovskite and the origin of ultralow-velocity zones. *Science*, *312*(5773), 564–565. https://doi.org/10.1126/science.1123442

McNamara, A. K. (2019). A review of large low shear velocity provinces and ultra low velocity zones. *Tectonophysics*, *760*, 199–220. https://doi.org/10.1016/j.tecto.2018.04.015

Mergner, V., Kupenko, I., Spiekermann, G., Petitgirard, S., Libon, L., Chariton, S., et al. (2021). Sound velocities in FeSi at lower mantle conditions and the origin of ultralow-velocity zones. *Geophysical Research Letters*, *48*(14), e2020GL092257. https://doi.org/10.1029/2020gl092257

Müller, G. (1985). The reflectivity method: A tutorial. *Journal of Geophysics*, *58*, 153–174.

Murakami, M., Hirose, K., Kawamura, K., Sata, N., & Ohishi, Y. (2004). Post-perovskite phase transition in $MgSiO_3$. *Science*, *304*(5672), 855–858. https://doi.org/10.1126/science.1095932

Niu, F., & Wen, L. (2001). Strong seismic scatterers near the core-mantle boundary west of Mexico. *Geophysical Research Letters*, *28*(18), 3557–3560. https://doi.org/10.1029/2001gl013270

Otsuka, K., & Karato, S.-I. (2012). Deep penetration of molten iron into the mantle caused by a morphological instability. *Nature*, *492*(7428), 243–246. https://doi.org/10.1038/nature11663

Pachhai, S., Dettmer, J., & Tkalčić, H. (2015). Ultra-low velocity zones beneath the Philippine and Tasman Seas revealed by a trans-dimensional Bayesian waveform inversion. *Geophysical Journal International*, *203*(2), 1302–1318. https://doi.org/10.1093/gji/ggv368

Pachhai, S., Li, M., Thorne, M. S., Dettmer, J., & Tkalčić, H. (2022). Internal structure of ultralow-velocity zones consistent with origin from a basal magma ocean. *Nature Geoscience*, *15*(1), 79–84. https://doi.org/10.1038/s41561-021-00871-5

Pachhai, S., Thorne, M. S., & Nissen-Meyer, T. (2022). Quantification of Small-scale heterogeneity at the core–mantle boundary using sample entropy of SKS and SPdKS synthetic waveforms. *Minerals*, *12*(7), 813. https://doi.org/10.3390/min12070813

Pachhai, S., Tkalčić, H., & Dettmer, J. (2014). Bayesian inference for ultralow velocity zones in the Earth's lowermost mantle: Complex ULVZ beneath the east of the Philippines. *Journal of Geophysical Research: Solid Earth*, *119*(11), 8346–8365. https://doi.org/10.1002/2014jb011067

Rawlinson, N., & Kennett, B. L. (2004). Rapid estimation of relative and absolute delay times across a network by adaptive stacking. *Geophysical Journal International*, *157*(1), 332–340. https://doi.org/10.1111/j.1365-246x.2004.02188.x

Revenaugh, J., & Meyer, R. (1997). Seismic evidence of partial melt within a possibly ubiquitous low-velocity layer at the base of the mantle. *Science*, *277*(5326), 670–673. https://doi.org/10.1126/science.277.5326.670

Ritsema, J., Deuss, a.A., Van Heijst, H., & Woodhouse, J. (2011). S40RTS: A degree-40 shear-velocity model for the mantle from new Rayleigh wave dispersion, teleseismic traveltime and normal-mode splitting function measurements. *Geophysical Journal International*, *184*(3), 1223–1236. https://doi.org/10.1111/j.1365-246x.2010.04884.x

Rondenay, S., Cormier, V. F., & Van Ark, E. M. (2010). SKS and SPdKS sensitivity to two-dimensional ultralow-velocity zones. *Journal of Geophysical Research*, *115*(B4), B04311. https://doi.org/10.1029/2009jb006733

Rondenay, S., & Fischer, K. M. (2003). Constraints on localized core-mantle boundary structure from multichannel, broadband SKS coda analysis. *Journal of Geophysical Research*, *108*(B11), 2537. https://doi.org/10.1029/2003jb002518

Ross, A., Thybo, H., & Solidilov, L. (2004). Reflection seismic profiles of the core-mantle boundary. *Journal of Geophysical Research*, *109*(B8). https://doi.org/10.1029/2003jb002515

Rost, S., Earle, P. S., Shearer, P. M., Frost, D. A., & Selby, N. D. (2015). Seismic detections of small-scale heterogeneities in the deep Earth. In A. Khan & F. Deschamps (Eds.), *The Earth's heterogeneous mantle: A geophysical, geodynamical, and geochemical perspective* (pp. 367–390). Springer International Publishing. https://doi.org/10.1007/978-3-319-15627-9

Rost, S., Garnero, E. J., & Stefan, W. (2010). Thin and intermittent ultralow-velocity zones. *Journal of Geophysical Research*, *115*(B6), B06312. https://doi.org/10.1029/2009jb006981

Rost, S., Garnero, E. J., & Williams, Q. (2006). Fine-scale ultralow-velocity zone structure from high-frequency seismic array data. *Journal of Geophysical Research*, *111*(B9), B09310. https://doi.org/10.1029/2005jb004088

Rost, S., Garnero, E. J., Williams, Q., & Manga, M. (2005). Seismological constraints on a possible plume root at the core–mantle boundary. *Nature*, *435*(7042), 666–669. https://doi.org/10.1038/nature03620

Rost, S., & Revenaugh, J. (2001). Seismic detection of rigid zones at the top of the core. *Science*, *294*(5548), 1911–1914. https://doi.org/10.1126/science.1065617

Rost, S., & Revenaugh, J. (2003). Small-scale ultralow-velocity zone structure imaged by ScP. *Journal of Geophysical Research*, *108*(B1). https://doi.org/10.1029/2001jb001627

Rost, S., & Revenaugh, J. (2004). Small-scale changes of core-mantle boundary reflectivity studied using core reflected PcP. *Phys., Earth and Planet. Int.*, *145*(1–4), 19–36. https://doi.org/10.1016/j.pepi.2004.02.008

Rost, S., & Thomas, C. (2002). Array seismology: Methods and applications. *Reviews of Geophysics*, *40*(3), 2-1–2-27. https://doi.org/10.1029/2000rg000100

Rost, S., Thorne, M. S., & Garnero, E. J. (2006). Imaging global seismic phase arrivals by stacking array processed short-period data. *Seismological Research Letters*, *77*(6), 697–707. https://doi.org/10.1785/gssrl.77.6.697

Shearer, P. M. (2007). Seismic scattering in the deep Earth. *Treatment of Geophysics*, *1*, 695–730.

Shearer, P. M. (2019). *Introduction to seismology*. Cambridge University Press.

Shim, S. H., Duffy, T. S., Jeanloz, R., & Shen, G. (2004). Stability and crystal structure of $MgSiO_3$ perovskite to the core-mantle boundary. *Geophysical Research Letters*, *31*(10). https://doi.org/10.1029/2004gl019639

Sigloch, K. (2011). Mantle provinces under North America from multifrequency P wave tomography. *Geochemistry, Geophysics, Geosystems*, *12*(2). https://doi.org/10.1029/2010gc003421

Simmons, N. A., Forte, A. M., Boschi, L., & Grand, S. P. (2010). GyPSuM: A joint tomographic model of mantle density and seismic wave speeds. *Journal of Geophysical Research*, *115*(B12), B12310. https://doi.org/10.1029/2010jb007631

Thorne, M. S., & Garnero, E. J. (2004). Inferences on ultralow-velocity zone structure from a global analysis of SPdKS waves. *Journal of Geophysical Research*, *109*(B8). https://doi.org/10.1029/2004jb003010

Thorne, M. S., Garnero, E. J., Jahnke, G., Igel, H., & McNamara, A. K. (2013). Mega ultra low velocity zone and mantle flow. *Earth and Planetary Science Letters*, *364*, 59–67. https://doi.org/10.1016/j.epsl.2012.12.034

Thorne, M. S., Leng, K., Pachhai, S., Rost, S., Wicks, J., & Nissen-Meyer, T. (2021). The most parsimonious ultralow-velocity zone distribution from highly anomalous SPdKS waveforms. *Geochemistry, Geophysics, Geosystems*, *22*(1), e2020GC009467. https://doi.org/10.1029/2020gc009467

Thorne, M. S., Pachhai, S., Leng, K., Wicks, J. K., & Nissen-Meyer, T. (2020). New candidate ultralow-velocity zone locations from highly anomalous SPdKS waveforms. *Minerals*, *10*(3), 211. https://doi.org/10.3390/min10030211

Thorne, M. S., Takeuchi, N., & Shiomi, K. (2019). Melting at the edge of a slab in the deepest mantle. *Geophysical Research Letters*, *46*(14), 8000–8008. https://doi.org/10.1029/2019gl082493

Thybo, H., Ross, A. R., & Egorkin, A. (2003). Explosion seismic reflections from the Earth's core. *Earth and Planetary Science Letters*, *216*(4), 693–702. https://doi.org/10.1016/s0012-821x(03)00532-6

Trampert, J., & van Heijst, H. J. (2002). Global azimuthal anisotropy in the transition zone. *Science*, *296*(5571), 1297–1299. https://doi.org/10.1126/science.1070264

Wicks, J., Jackson, J., & Sturhahn, W. (2010). Very low sound velocities in iron-rich (Mg, Fe) O: Implications for the core-mantle boundary region. *Geophysical Research Letters*, *37*(15). https://doi.org/10.1029/2010gl043689

Wicks, J. K., Jackson, J. M., Sturhahn, W., & Zhang, D. (2017). Sound velocity and density of magnesiowüstites: Implications for ultralow-velocity zone topography. *Geophysical Research Letters*, *44*(5), 2148–2158. https://doi.org/10.1002/2016gl071225

Williams, Q., & Garnero, E. J. (1996). Seismic evidence for partial melt at the base of Earth's mantle. *Science*, *273*(5281), 1528–1530. https://doi.org/10.1126/science.273.5281.1528

Wookey, J., Kendall, J.-M., & Rümpker, G. (2005). Lowermost mantle anisotropy beneath the north Pacific from differential S—ScS splitting. *Geophysical Journal International*, *161*(3), 829–838. https://doi.org/10.1111/j.1365-246x.2005.02623.x

Wysession, M. E., Langenhorst, A., Fouch, M. J., Fischer, K. M., Al-Eqabi, G. I., Shore, P. J., & Clarke, T. J. (1999). Lateral variations in compressional/shear velocities at the base of the mantle. *Science*, *284*(5411), 120–125. https://doi.org/10.1126/science.284.5411.120

Yu, S., & Garnero, E. J. (2018). Ultralow velocity zone locations: A global assessment. *Geochemistry, Geophysics, Geosystems*, *19*(2), 396–414. https://doi.org/10.1002/2017gc007281

Yuan, K., & Romanowicz, B. (2017). Seismic evidence for partial melting at the root of major hot spot plumes. *Science*, *357*(6349), 393–397. https://doi.org/10.1126/science.aan0760

Zhao, C., Garnero, E. J., Li, M., McNamara, A., & Yu, S. (2017). Intermittent and lateral varying ULVZ structure at the northeastern margin of the Pacific LLSVP. *Journal of Geophysical Research: Solid Earth*, *122*(2), 1198–1220. https://doi.org/10.1002/2016jb013449